Journal of Geophysical Research: Earth Surface

RESEARCH ARTICLE
10.1029/2017JF004416

Distinct Thresholds for the Initiation and Cessation of Aeolian Saltation From Field Measurements

Raleigh L. Martin[1] and **Jasper F. Kok**[1]

[1]Department of Atmospheric and Oceanic Sciences, University of California, Los Angeles, CA, USA

Key Points:
- We provide the first field-based evidence for separate fluid and impact thresholds in aeolian saltation
- Saltation occurrence is mediated by both thresholds, but fluid (impact) threshold dominates during infrequent (near-continuous) transport
- Both thresholds are important for high-frequency saltation prediction, but long-term aeolian fluxes are governed mostly by impact threshold

Supporting Information:
- Supporting Information S1
- Data Set S1

Correspondence to:
R. L. Martin,
raleighmartin@gmail.com

Citation:
Martin, R. L., & Kok, J. F. (2018). Distinct thresholds for the initiation and cessation of aeolian saltation from field measurements. *Journal of Geophysical Research: Earth Surface*, *123*, 1546–1565. https://doi.org/10.1029/2017JF004416

Received 19 JUL 2017
Accepted 24 MAY 2018
Accepted article online 19 JUN 2018
Published online 17 JUL 2018

Abstract Wind-blown sand and dust models depend sensitively on the threshold wind stress. However, laboratory and numerical experiments suggest the coexistence of distinct *fluid* and *impact* thresholds for the initiation and cessation of aeolian saltation, respectively. Because aeolian transport models typically use only a single threshold, existence of separate higher fluid and lower impact thresholds complicates the prediction of wind-driven transport. Here we extend the statistical *Time Frequency Equivalence Method* to derive the first field-based estimates of distinct fluid and impact thresholds from high-frequency wind and saltation measurements at three field sites. Our measurements show that when saltation is mostly inactive, its instantaneous occurrence is governed primarily by wind exceedance of the fluid threshold. As saltation activity increases, so too does the relative importance of the impact threshold, until it dominates under near-continuous transport conditions. Although both thresholds are thus important for high-frequency saltation prediction, our results suggest that the time-averaged saltation flux is primarily governed by the impact threshold.

Plain Language Summary In our article, we address a core issue in studies of Earth and planetary surface processes: What is the minimum or *threshold* wind speed for moving sediment? Predictions for sediment transport movement by air and water depend sensitively on the choice of thresholds in models. In the case of wind-blown sand particles, the story is complicated by the presence of separate *fluid* and *impact* thresholds for the respective initiation and cessation of transport. Using a comprehensive field data set, we provide the first field-based determination of distinct fluid and impact thresholds, and we demonstrate how both thresholds together are needed to predict the instantaneous occurrence of wind-blown sand transport. We also find that models for large-scale processes driven by wind-blown sand—atmospheric dust aerosol generation, transport of wind-borne nutrients, erosion of agricultural soils, and formation of protective coastal dunes—should primarily use the impact threshold rather than the fluid threshold.

1. Introduction

Determining the threshold wind shear stress for the occurrence of wind-driven (*aeolian*) sand transport has been a central challenge for studies of planetary, coastal, and desert aeolian processes (e.g., Bagnold, 1941; Iversen & White, 1982; Shao & Lu, 2000). In desert and semiarid environments, the aeolian saltation threshold regulates the frequency of topsoil erosion and mineral dust emission (e.g., Rice et al., 1999). Where sand dunes and ripples are present, the saltation threshold governs the frequency of migration of these bedforms (e.g., Fryberger et al., 1979). Recent aeolian transport studies indicate that sand flux scales linearly (e.g., Ho et al., 2011; Martin & Kok, 2017) with wind stress in excess of the saltation threshold, so shifts in the presumed threshold value can substantially change predictions of the total sand saltation flux and associated dust emissions (e.g., Kok et al., 2014; Sherman et al., 2013; Webb et al., 2016). Uncertainty in threshold is therefore a major issue for studies relating aeolian transport observations to atmospheric conditions on Earth (e.g., Lindhorst & Betzler, 2016), Mars (e.g., Ayoub et al., 2014; Bridges et al., 2012), and other planetary surfaces (e.g., Lorenz & Zimbelman, 2014).

Despite the central importance of the saltation threshold in predicting sand and dust fluxes, there remains a lack of agreement over the best way to model or even measure this threshold (Barchyn & Hugenholtz, 2011). Most predictive equations for saltation usually include only a single threshold value (Barchyn, Martin, et al., 2014). In studies of saltation-driven dust emission (e.g., Marticorena & Bergametti, 1995), such a single threshold is typically chosen as the *fluid* or *static* threshold shear stress τ_{ft} for initiating saltation transport solely by aerodynamic forces (e.g., Iversen & White, 1982). Other studies of saltation dynamics and associated dune evolution processes (e.g., Andreotti, 2004; Durán et al., 2011; Fryberger et al., 1979; Ho et al., 2011; Sherman & Li, 2012; Sørensen, 2004; Ungar & Haff, 1987) instead use a separate, lower *impact* or *dynamic*

threshold shear stress τ_{it} required to sustain saltation through saltator impacts with the sand bed. This impact threshold has been hypothesized to equal the rate of momentum dissipation at the surface (Owen, 1964), which is controversial (Kok et al., 2012) but for which there is now limited experimental support (Walter et al., 2014).

Based on the role of the impact threshold in the steady state saltation momentum balance, most recent saltation models use impact threshold alone as the zero-intercept value for the saltation flux law (Creyssels et al., 2009; Martin & Kok, 2017; Ungar & Haff, 1987). However, recent studies have argued for the need to simulate the path dependence of saltation flux responses to turbulent wind fluctuations around both impact and fluid thresholds (Kok, 2010a, 2010b). The ratio of impact and fluid thresholds governing this hysteresis depends primarily on the particle-fluid density ratio, which determines the relative contributions of particle impacts and direct fluid lifting to particle entrainment (Kok, 2010b; Pähtz & Durán, 2017). On Earth, the experimentally (Bagnold, 1937; Chepil, 1945; Iversen & Rasmussen, 1994) and numerically (Kok, 2010b) predicted ratio of impact and fluid threshold shear velocities u_{*it}/u_{*ft} is approximately 0.82, whereas u_{*it}/u_{*ft} is predicted to be as low as 0.1 on Mars (Kok, 2010a).

Though numerical and experimental studies predict fluid and impact thresholds, field studies have not yet confirmed the existence of these two separate thresholds, let alone determined which should be used for modeling sand and dust flux. One possible approach to field-based determination of fluid and impact thresholds is to directly examine the correlation between the wind speed and the occurrence of saltation onset and cessation events. However, the signal of dual thresholds revealed by such an approach is typically overwhelmed by the noise in highly variable wind and saltation measurements (Barchyn & Hugenholtz, 2011; Martin et al., 2013). Comparisons of saltation flux measurements to time series of wind speed (e.g., Davidson-Arnott et al., 2005; Davidson-Arnott & Bauer, 2009; Wiggs, Atherton, & Baird, 2004) or momentum flux (e.g., Sterk et al., 1998) display a poor correlation at short time scales due to spatial separation between saltation and wind measurements (Baas, 2008), variability in surface grain configurations (Z. Li et al., 2008; Nickling, 1988), small-scale fluctuations in the turbulent winds driving saltation (Carneiro et al., 2015), and decoupling of saltation and wind systems (Paterna et al., 2016). Therefore, such a deterministic correlation-based approach to measuring fluid and impact thresholds in the field is difficult.

Here we instead adopt a statistical approach to determine distinctive fluid and impact thresholds in aeolian saltation from extensive high-frequency field measurements of aeolian transport at three field sites. In the following sections, we develop a *dual threshold hypothesis* for how fluid and impact thresholds determine the effective threshold governing the frequency of saltation activity (section 2), describe methods for calculating these saltation activities and effective thresholds from field measurements (section 3), use these calculations to test the dual threshold hypothesis and derive field-based estimates of separate fluid and impact thresholds (section 4), discuss the role of fluid and impact thresholds in modeling sand and dust fluxes (section 5), and conclude with a summary of this work (section 6).

2. Theory

We expect the occurrence of aeolian saltation transport to be governed by both the fluid and impact thresholds, based on the relative importance of transport initiation versus cessation. In this section, we describe how, over time intervals of intermittent saltation that include many threshold crossings, the combined contributions of τ_{ft} and τ_{it} should produce an intermediate *effective* threshold stress τ_{th} that varies systematically with the fraction of time f_Q that saltation is active. To demonstrate this theory, we utilize sample time series of wind speed u and this *saltation activity* f_Q (i.e., Davidson-Arnott et al., 2012) from our field campaigns. We will describe methods for obtaining these time series in section 3.

2.1. Regulation of Saltation Occurrence by Fluid and Impact Thresholds

To illustrate the role of dual thresholds in regulating the occurrence of saltation, we consider three sample time series (Figure 1) of near-surface (anemometer height $z_U \approx 0.5$ m) horizontal wind speed $u(t)$ straddling fluid and impact threshold wind speeds, u_{ft} and u_{it}, respectively, corresponding to τ_{ft} and τ_{it}. As we will describe further in section 3, we obtained $u(t)$ time series from sonic anemometers mounted at heights $z_U \approx 0.5$ m above flat, erodible sand surfaces at three distinctive field sites. We obtained fluid and impact thresholds through extension of the statistical *Time Frequency Equivalence Method* (*TFEM*; Stout & Zobeck,

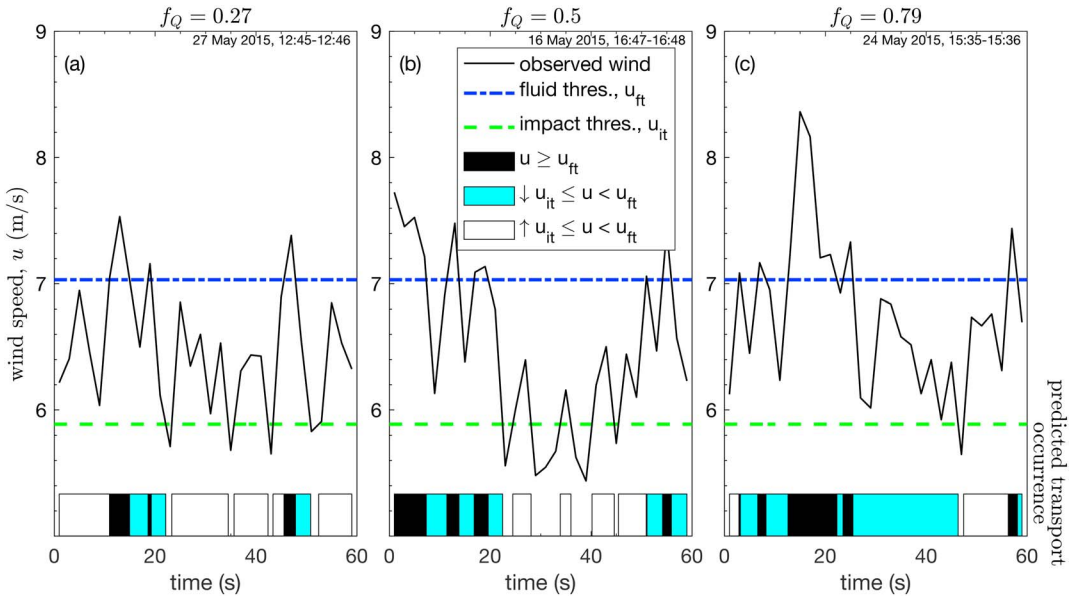

Figure 1. Illustration of variations in wind speed u and predicted saltation occurrence for time intervals with (a) low ($f_Q = 0.27$), (b) medium ($f_Q = 0.5$), and (c) high ($f_Q = 0.79$) observed transport activity at the Oceano field site (introduced in section 3). Blue and green dashed lines indicate respective fluid and impact threshold wind speeds, u_{ft} and u_{it}. Black bars at the bottom of each panel refer to times when $u \geq u_{ft}$. Both cyan and white bars refer to *intermittent zone* times when $u_{it} \leq u < u_{ft}$, but they are distinguished between times approached from above u_{ft} (cyan) versus from below u_{it} (white). Black and cyan bars thus indicate times of predicted transport occurrence. As saltation activity f_Q increases from panels a to c, the intermittent zone is increasingly approached from above and decreasingly from below.

1997); such threshold values are previewed in Figure 1 simply to demonstrate the theory underlying these threshold determination methods.

Figure 1 shows expectations for the occurrence of saltation transport when $u(t)$ is close to u_{ft} and u_{it}. When $u \geq u_{ft}$, we unambiguously expect saltation transport to occur; conversely, when $u < u_{it}$, transport should not occur. Ambiguity in prediction of saltation occurrence arises in cases where $u_{it} \leq u < u_{ft}$. In this *intermittent zone*, saltation occurrence should depend on whether saltation transport was initiated (i.e., $u \geq u_{ft}$) more recently than it was terminated (i.e., $u < u_{it}$; Kok, 2010b).

Over time intervals covering multiple threshold crossings, we expect the frequency of saltation activity f_Q to partially depend on the fraction of intermittent zone winds (i.e., $u_{it} \leq u < u_{ft}$) that are approached from below ($u < u_{it}$) versus from above ($u \geq u_{ft}$). Figure 1 illustrates the nature of these intermittent zone events for three distinctive cases of measured infrequent (panel a: $f_Q = 0.27$), moderate (panel b: $f_Q = 0.5$), and frequent (panel c: $f_Q = 0.79$) saltation activity. (Methods for calculating f_Q from measurements will be described in section 3.) When the intermittent zone is mostly approached from below (i.e., from a state of nontransport), saltation is mostly limited by the occurrence of initiation events, for which $u \geq u_{ft}$ (Figure 1a). As such, near the no-saltation limit $f_Q \to 0$, saltation activity is controlled primarily by wind exceedance of the fluid threshold. In the contrasting case when the intermittent zone is mostly approached from above ($u \geq u_{ft}$; i.e., from a state of transport), saltation will mostly be sustained as long as $u \geq u_{it}$ (Figure 1c). Consequently, near the continuous saltation limit $f_Q \to 1$, saltation occurrence is controlled primarily by wind exceedance of the impact threshold. Otherwise, for cases of intermittent zone winds originating equally from starting points above u_{ft} and below u_{it} (Figure 1b), expectations for saltation occurrence will be somewhere between these two end-member cases. In general, the examples in Figure 1 suggest that with an increasing fraction of intermittent zone winds originating from $u \geq u_{ft}$ relative to $u < u_{it}$, saltation occurrence will move away from the $f_Q \to 0$ limit of u_{ft} control toward the $f_Q \to 1$ limit of u_{it} control.

2.2. Dual Threshold Hypothesis for Saltation Activity

The three cases presented in Figure 1 suggest that increasing f_Q corresponds to saltation occurrence being increasingly controlled by the impact rather than the fluid threshold. Based on this observation, we

Table 1
Fluid and Impact Threshold Stresses (τ_{ft} and τ_{it}, Respectively), Threshold Stress Ratios (τ_{it}/τ_{ft}), Shear Velocities ($u_{*,\,ft}$ and $u_{*,\,it}$, Respectively), and Shear Velocity Threshold Ratios $u_{*,\,it}/u_{*,\,ft}$ for Primary Analysis With δt = 2 s Averaging Interval and Δt = 1-min Analysis Interval

Site	d_{50} (mm)	d_{10} (mm)	d_{90} (mm)	τ_{ft} (Pa)	τ_{it} (Pa)	τ_{it}/τ_{ft}	$u_{*,\,ft}$ (m/s)	$u_{*,\,it}$ (m/s)	$u_{*,\,it}/u_{*,\,ft}$	$\tau_{th,\,flux}$ (Pa)
Jericoa coara	0.526 ± 0.037	0.097 ± 0.012	0.847 ± 0.037	0.168 ± 0.004	0.111 ± 0.002	0.661 ± 0.019	0.380 ± 0.005	0.309 ± 0.003	0.813 ± 0.018	0.135 ± 0.015
Rancho Guadalupe	0.533 ± 0.026	0.219 ± 0.035	0.839 ± 0.034	0.147 ± 0.006	0.110 ± 0.002	0.745 ± 0.035	0.347 ± 0.009	0.300 ± 0.003	0.863 ± 0.027	0.110 ± 0.021
Oceano	0.398 ± 0.070	0.190 ± 0.032	0.650 ± 0.075	0.125 ± 0.001	0.088 ± 0.001	0.701 ± 0.008	0.321 ± 0.001	0.269 ± 0.002	0.837 ± 0.007	0.094 ± 0.006

Note. Median d_{50}, 10th percentile d_{10}, and 90th percentile d_{90} grain diameters of surface particles and threshold stresses from flux-law fits $\tau_{th,\,flux}$ at each site (Martin & Kok, 2017) are included for reference.

consider how a statistically defined effective threshold wind shear stress τ_{th}, which refers to the average threshold wind stress above which saltation is expected to occur (e.g., Stout & Zobeck, 1997), reflects the relative contributions of fluid and impact threshold stresses, τ_{ft} and τ_{it}, with increasing f_Q. In particular, we propose a dual threshold hypothesis, in which $\tau_{th} = \tau_{ft}$ in the initiation-limited rare transport case ($f_Q \to 0$), $\tau_{th} = \tau_{it}$ in the cessation-limited continuous transport case ($f_Q \to 1$), and τ_{th} decreases linearly with f_Q between these two limits:

$$\tau_{th} = f_Q \tau_{it} + (1 - f_Q)\tau_{ft}. \quad (1)$$

This hypothesis is consistent with the work of Schönfeldt (2004), who predicted an analogous gradual decrease in effective threshold with increasing mean wind speed (rather than saltation activity) in stochastic simulations of wind speed fluctuating around fluid and impact thresholds. If correct, equation (1) offers a way to determine the impact and fluid thresholds from measurements of effective threshold and saltation activity. Conversely, equation (1) could also allow for prediction of saltation activity from wind time series and known impact and fluid thresholds.

3. Methods

3.1. Field Deployments

To evaluate our dual threshold hypothesis that effective threshold is partitioned between fluid and impact thresholds depending on the saltation activity (equation (1)), we analyze here simultaneous high-frequency measurements of active saltation and wind at three field sites: Jericoacoara, Ceará, Brazil (2.7969°S, 40.4837°W); Rancho Guadalupe, California, United States (34.9592°N, 120.6431°W); and Oceano, California, United States (35.0287°N, 120.6277°W). All field sites contain mostly flat, unvegetated, sand-covered surfaces, with distinctive sediment size distributions. We determined median, 10th percentile, and 90th percentile grain diameters (d_{50}, d_{10}, and d_{90}, respectively), through Camsizer optical grain size analysis (Jerolmack et al., 2011) of surface grab samples collected each day at each field site. For reference, Table 1 lists the mean values of d_{50}, d_{10}, and d_{90} for each site, though we note that surface grain diameters displayed some variation from day to day (Martin et al., 2018).

During each field campaign, multiple (three to nine) Wenglor optical sensors (Barchyn, Hugenholtz, et al., 2014) at heights from the bed surface up to ≈0.3 m counted saltating particles (at 25 Hz), which we combine into vertically integrated saltation particle count rates N (Figure 2a). Wenglors were mounted on one or two fixed vertical arrays (Martin et al., 2018), with a maximum spanwise separation among sensors of 1.3 m. Though numbers and heights of Wenglors, and thus corresponding measurements of total saltation number counts (Bauer & Davidson-Arnott, 2014; Hilton et al., 2017), varied among field sites and deployment days (Martin et al., 2018), we are concerned here only with the frequency of occurrence of saltation. Based on the observed constant vertical shape of saltation profiles (Martin & Kok, 2017) and the fact that Wenglor sensor saturation (e.g., Hugenholtz & Barchyn, 2011; Sherman et al., 2011) appears to be absent (Martin et al., 2018), we assume that differences in Wenglor heights among deployments affect only the possibility of false negatives (i.e., potential under-detection of saltation frequency), and we correct for this by treating particle arrivals as a Poisson process (see Appendix A).

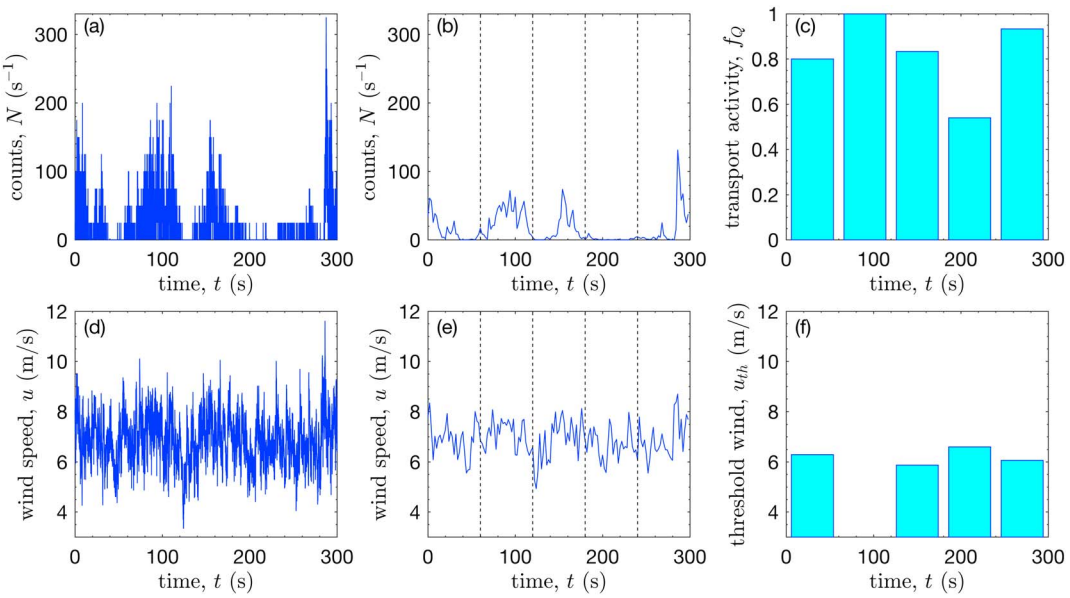

Figure 2. Sample measurements (Rancho Guadalupe, 24 March 2015, 13:31–13:36) to illustrate methods for calculating saltation transport activity f_Q and effective threshold wind speed u_{th}. (a) Time series of total particle counts rate N. (b) δt = 2 s interval-averaged N time series. Dashed lines indicate Δt = 1 min analysis intervals. (c) Transport activities f_Q, calculated as fraction of δt increments in each Δt for which $N > 0$, and corrected for false negatives. (d) Time series of streamwise wind speed u. (e) δt = 2 s interval-averaged u. Dashed lines again indicate Δt. (f) Resulting values of threshold wind speed u_{th} calculated by equation (2) from corresponding f_Q and wind speed distributions Φ_u for each Δt. u_{th} is undefined for t= 60–120 s when f_Q = 1.

In addition to Wenglor saltation sensors, a sonic anemometer at height $z_U \approx 0.5$ m (Martin et al., 2018) measured three-dimensional wind velocity (25 Hz at Jericoacoara and Rancho Guadalupe, 50 Hz at Oceano; Figure 2d). To account for the small variation in wind direction during periods of active saltation (Martin & Kok, 2017), we apply standard anemometer rotation protocols (van Boxel et al., 2004) to successive 30-min intervals of wind data to obtain saltation-aligned time series for streamwise wind speed u. Though our field deployments (described further in Martin et al., 2018) included anemometers at multiple heights, we choose here to use measurements from only the lowest anemometer (i.e., $z_U \approx 0.5$ m) at each site, because we expect these measurements to be most representative of wind fluctuations at the sand surface. Furthermore, we observed no significant difference in the relevant wind statistics between $z_U \approx 0.5$ m and $z_U \approx 1.0$ anemometers (Martin & Kok, 2017). Based on instrument positioning, wind measurements described in this analysis are vertically offset from saltation measurements by ≈0.2–0.5 m. At Jericoacoara and Rancho Guadalupe, wind measurements are additionally separated from saltation measurements by ≈1 m in the spanwise direction, whereas they are spanwise colocated at Oceano (Martin et al., 2018).

3.2. Calculating Effective Thresholds

To calculate saltation activity f_Q and effective threshold wind speed u_{th}, we apply δt = 2 s interval averaging to saltation (Figure 2b) and wind (Figure 2e) time series, then we subdivide these data into Δt = 1-min analysis intervals. Within each analysis interval, we calculate saltation activity f_Q as the fraction of δt increments within Δt for which N is nonzero (Figure 2c). Due to counting uncertainty for the small sampling volume of Wenglor sensors counting the passage of individual particles over short time intervals, we apply a slight correction to f_Q to account for the possibility of false negatives (see Appendix A). For each Δt, we then calculate effective threshold wind speed u_{th} by applying the TFEM (Davidson-Arnott et al., 2012; Sherman et al., 2017; Stout, 2004; Stout & Zobeck, 1997; Wiggs, Atherton, & Baird, 2004):

$$u_{th} = \Phi_u(1 - f_Q), \tag{2}$$

where $\Phi_u(1 - f_Q)$ is the value in the cumulative distribution of wind speeds Φ_u corresponding to the time fraction of inactive saltation, $1 - f_Q$ (Figure 2f). When calculating Φ_u for each Δt, we use the δt-averaged u values,

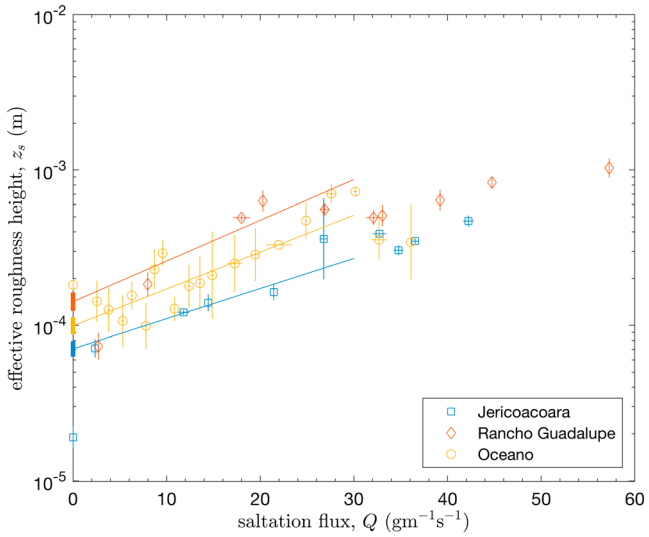

Figure 3. Comparison of effective roughness height z_s versus saltation flux Q at each field site. Values are calculated over 30-min intervals and combined into bins by Q. We estimate z_0 as the zero intercept of the linear fit of $\ln(z_s)$ versus Q at each site for $Q \leq 30$ g·m^{-1}·s^{-1}, indicated by the solid lines. Resulting calculated z_0 values for each site are shown as thick vertical bars at $Q = 0$ g·m^{-1}·s^{-1}. The vertical range of these bars corresponds to uncertainties in z_0 as determined by the linear fits.

in correspondence with our methods for calculating f_Q. We choose the averaging interval $\delta t = 2$ s based on the typical response time of saltation to turbulent wind fluctuations (e.g., Anderson & Haff, 1988; Ma & Zheng, 2011; McEwan & Willetts, 1991), and we choose the analysis interval $\Delta t = 1$ min to represent the typical oscillation period for large-scale structures in an atmospheric boundary layer (e.g., Guala et al., 2011). We note here that due to the spatial separation of wind and saltation measurements, we cannot directly relate individual high-frequency wind gusts to individual occurrences of saltation. Instead, we assume, based on the correspondence of low-frequency wind fluctuations across a wide range of heights (e.g., Marusic et al., 2010), that measured wind fluctuations over Δt are statistically representative of the wind experienced by the measured saltating particles.

To account for statistical variability and facilitate uncertainty estimation, we group effective threshold wind speed u_{th} values computed over individual Δt intervals into f_Q bins (see Appendix B). We then convert binned u_{th} values into effective threshold shear velocities $u_{*,th}$ and stresses τ_{th} by the law of the wall and the standard τ-u_* relationship:

$$u_{th} = \frac{u_{*,th}}{\kappa} \ln\left(\frac{z_U}{z_0}\right), \tag{3}$$

$$\tau_{th} = \rho_f u_{*,th}^2, \tag{4}$$

where z_0 is aerodynamic roughness height, $\kappa \approx 0.4$ is the von Karman parameter, and ρ_f is air density determined from the mean temperature at each site (Martin & Kok, 2017). We apply standard error propagation techniques to estimate uncertainties in resulting calculated $u_{*,th}$ and τ_{th} values (Appendix B).

We note here that our estimates for threshold shear velocity and stress (equations (3) and (4)) depend on application of the law of the wall to streamwise wind speed u rather than on application of the Reynolds stress to the covariance of streamwise and vertical winds. We use the law of the wall for two main reasons. First, the TFEM for computing effective thresholds depends on examination of time series of horizontal wind speed and transforming the resulting u_{th} to $u_{*,th}$, and τ_{th} is much more straightforward by the law of the wall (equations (3) and (4)) than it would be by the Reynolds stress. Second, over $\Delta t = 1$ min analysis intervals, the Reynolds stress method inadequately captures the full range of turbulence structures (van Boxel et al., 2004, Figure 3). In contrast, the horizontal wind speed provides a more reliable way to estimate the wind stress associated with saltation over short time intervals, as it is the horizontal drag applied by the wind that most strongly determines the saltation flux at short time scales (Sterk et al., 1998). Analyses by Martin et al. (2013, Figure 4) demonstrate the clear advantage of the law of the wall over the Reynolds stress for $\Delta t = 1$ min. We further justify the applicability of the law of the wall for threshold shear velocity and shear stress calculations in the subsections below.

3.3. Applicability of the Law of the Wall

There are three possible issues in applying the law of the wall (equation (3)) to convert from threshold wind speeds to shear velocities and shear stresses, which could have important implications for the application of thresholds in predicting saltation flux (e.g., Rasmussen & Sørensen, 1999). First, the law of the wall is only strictly valid for unidirectional winds within a neutrally stable atmospheric boundary layer (e.g., Frank & Kocurek, 1994), but we frequently observe unstable wind conditions. Second, the law of the wall requires time averaging of the wind speed over a sufficiently long time period to capture the full range of turbulence variability (e.g., van Boxel et al., 2004), but we apply equation (3) to threshold wind speeds u_{th} obtained from quasi-instantaneous values within the wind speed distribution, which do not represent time averages. Third, measured roughness height is known to change systematically with saltation intensity (e.g., Sherman, 1992), but we use a constant z_0 in equation (3). We address each of these issues in the subsections below.

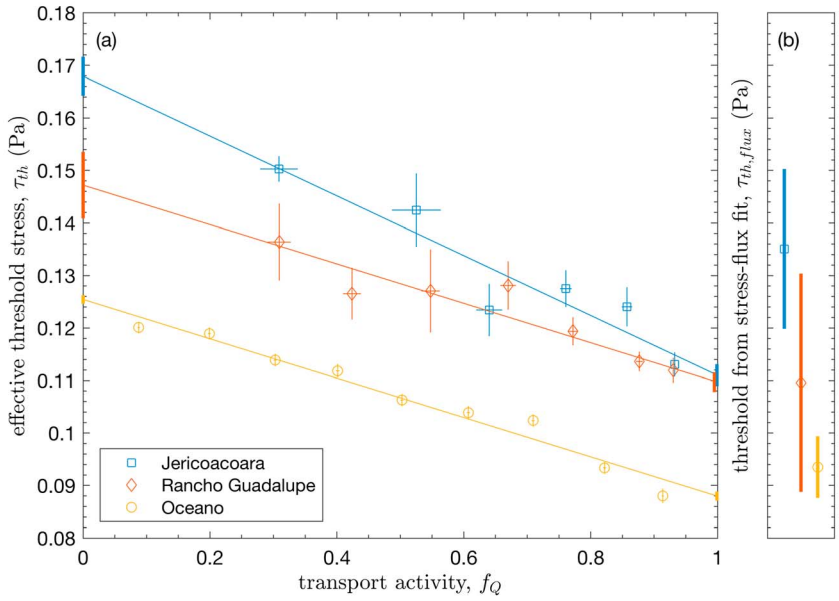

Figure 4. (a) Effective threshold stress τ_{th} versus saltation transport activity f_Q. Color-coded lines show least squares fits (equation (6)) at each field site. Vertical bars at $f_Q = 0$ and $f_Q = 1$ denote respective estimates of the fluid threshold τ_{ft} (equation (7)) and impact threshold τ_{it} (equation (8)) from the linear fit. (b) We estimate flux-based thresholds $\tau_{th,\ flux}$ for each field site by applying equation (10) to saltation flux measurements reported in Martin and Kok (2017). Specific values for τ_{ft}, τ_{it}, and $\tau_{th,\ flux}$ are listed in Table 1. Error bars correspond to 1 standard error.

3.3.1. Law of the Wall: Stability and Wind Direction

To address the need for unidirectional and neutrally stable conditions for application of the law of the wall, we note that during all periods of active saltation for which we perform threshold calculations, measured wind directions (i.e., θ) deviate by less than 20° from the mean sediment-transporting wind. Furthermore, stability parameter values (i.e., $|z/L|$) are always less than 0.2 during active saltation. (See Martin and Kok, 2017, for further explanation of these calculations.) For such unidirectional and neutrally stable winds during active saltation, law of the wall and Reynolds stress-based methods for computing the shear velocity are roughly equivalent (Salesky et al., 2012). This contrasts with observed wide variation in θ and $|z/L|$ during nonsaltation conditions (Martin & Kok, 2017), but our threshold calculations necessarily exclude such nonsaltation time intervals.

3.3.2. Law of the Wall: Averaging Time

To address the issue of time averaging, we note that independent measurements (Namikas et al., 2003) have demonstrated the convergence of law of the wall profiles over time periods as small as 10 s, shorter than our chosen $\Delta t = 1$ min. Furthermore, we make our threshold calculations only for anemometers mounted close to the bed surface (i.e., $z_U \approx 0.5$ m) that experience moderate to strong mean winds associated with saltation (i.e., $u \gtrsim 6$ m/s), suggesting reasonably rapid convergence of wind statistics (van Boxel et al., 2004).

However, we apply the law of the wall not to the mean wind over the $\Delta t = 1$ min analysis interval but to a single value (u_{th}) within a distribution Φ_u of winds over Δt; thus, the required measurement period for application of the law of the wall may be longer than our chosen Δt. To test for this possibility, we perform sensitivity analyses to assess possible changes in $u_{*,\ th}$ and τ_{th} with varying Δt. We find no systematic effect of varying Δt, suggesting that our choice of $\Delta t = 1$ min is sufficient for application of the law of the wall. We address this issue further in section 5.

3.3.3. Law of the Wall: Roughness Height

Now we address the selection of and possible saltation-induced variation in roughness height z_0 in equation (3). Because roughness height is known to increase with saltation intensity (e.g., Sherman, 1992), it is generally preferable to calculate z_0 from wind profiles measured during nonsaltation conditions. However, due to the occurrence of unstable wind profiles during nonsaltation conditions causing deviations from logarithmic profiles (section 3.3.1), we find that such measurements of z_0 display large variability over many orders of magnitude.

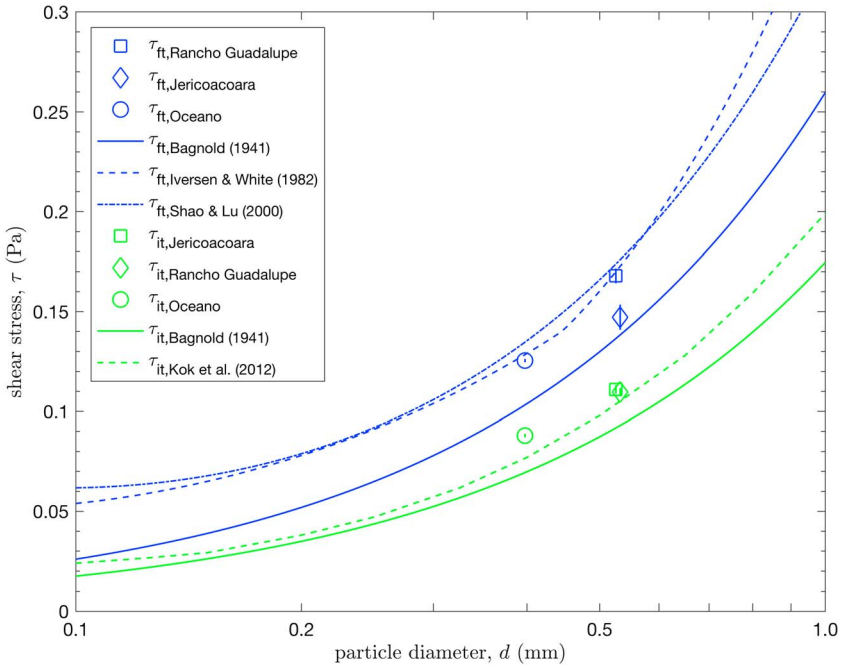

Figure 5. Comparison of measured fluid τ_{ft} and impact τ_{it} threshold shear stress values (Table 1) to predictions by particle diameter d for commonly used models: Bagnold (1941), Iversen and White (1982), and Shao and Lu (2000) for τ_{ft}; and Bagnold (1941) and Kok et al. (2012) for τ_{it}. We plot measured τ_{ft} and τ_{it} against median bed particle diameter d_{50} (Table 1) at each field site.

To avoid the problem of unstable profiles, we instead consider roughness heights measured during stronger winds, when near-surface wind profiles are closer to neutral stability. However, such stronger winds are associated with the occurrence of saltation and with a general increase in roughness height (e.g., Sherman, 1992). We therefore refer to these saltation-influenced roughness values as effective roughness heights z_s to distinguish them from the purely aerodynamic roughness z_0. As with z_0, the value for z_s can be determined by manipulating the law of the wall:

$$z_s = z_U \exp\left(-\frac{\kappa u}{u_{*,\mathrm{Re}}}\right), \tag{5}$$

where u here refers to the mean streamwise wind speed for the anemometer mounted at height z_U, and $u_{*,Re}$ is the shear velocity determined by the Reynolds stress method over a 30-min interval (Martin & Kok, 2017). We choose to calculate z_s from 30-min $u_{*,Re}$ values (instead of from the $\Delta t = 1$ min analysis intervals applied elsewhere in this paper), because $u_{*,Re}$ is ill defined at a time scale of 1 min (van Boxel et al., 2004), whereas 30-min intervals are long enough to account for most of the variability in turbulence structures but short enough to be minimally affected by mesoscale weather variability (e.g., Namikas, 2003; Sterk et al., 1998; Stull, 1988).

Comparing z_s values to saltation fluxes Q measured over corresponding intervals (see Martin and Kok (2017) for methods of estimating Q), we observe an increasing trend (Figure 3) consistent with expectations for saltation-induced roughness (Sherman, 1992). At each site, the logarithm of z_s increases linearly with Q up to $Q \approx 30$ g·m^{-1}·s^{-1}. Performing a linear fit to ln(z_s) versus Q over this range, we estimate z_0 as the zero-intercept (i.e., $Q = 0$) value of this fit, yielding values of $z_0 = 0.707 \times 10^{-4}$, 1.420×10^{-4}, and 0.993×10^{-4} m, for Jericoacoara, Rancho Guadalupe, and Oceano, respectively. Associated uncertainties in log space, that is, $\sigma_{\ln(z_0)}$, are 0.115, 0.137, and 0.128, for Jericoacoara, Rancho Guadalupe, and Oceano, respectively. Thus, Figure 3 demonstrates a way to estimate z_0 from the variation in z_s with Q.

Noting that saltation flux is typically small during periods of intermittent transport, we use our empirically derived z_0 values (Figure 3) for all threshold wind speed to shear velocity conversions (equation (3)). We

note that these z_0 values are somewhat larger than standard expectations of $z_0 = d_{50}/30$ (e.g., Nikuradse, 1933) =0.175×10^{-4}, 0.178×10^{-4}, and 0.133×10^{-4} m, for Jericoacoara, Rancho Guadalupe, and Oceano, respectively, or $z_0 \approx d_{50}/15$ (e.g., Sherman, 1992) =0.351×10^{-4}, 0.355×10^{-4}, and 0.265×10^{-4} m, for Jericoacoara, Rancho Guadalupe, and Oceano, respectively. This suggests that our measured z_0 values already include some effect of saltation- or topography-induced roughness. Nonetheless, based on observed limited variation in effective roughness height z_s with saltation transport activity f_Q at the Oceano field site (supporting information Figure S1), we believe that it is reasonable to use these calculated z_0 values for all shear velocity conversions in this study.

4. Results

To evaluate our hypothesis for dual threshold control of saltation activity and the effective saltation threshold (equation (1)), we use the methods described in section 3 to calculate effective threshold stresses and saltation activities at our three field sites. Due to the distinctive sand properties at each field site, we analyze the effective thresholds and saltation activities for each site separately.

4.1. Fluid and Impact Thresholds

As predicted by equation (1), we find that the effective threshold stress τ_{th} decreases linearly with saltation activity f_Q at each of the field sites (Figure 4a). To quantify this trend, we perform a linear fit to τ_{th} versus f_Q, that is,

$$\tau_{th} = a + bf_Q, \tag{6}$$

where a is the fitting intercept and b is the fitting slope. Based on uncertainties in these linear fitting parameters, we find that the observed decline in τ_{th} with f_Q is extremely unlikely by random chance alone ($p < 10^{-6}$). Based on this linear fit, we also calculate fluid and impact threshold stresses, τ_{ft} and τ_{it}, from the limiting effective threshold values for no transport ($f_Q \rightarrow 0$) and continuous transport ($f_Q \rightarrow 1$) in equation (1), that is,

$$\tau_{ft} = a, \tag{7}$$

$$\tau_{it} = a + b. \tag{8}$$

We follow standard error propagation methods (Bevington & Robinson, 2003) to determine uncertainties in τ_{ft} and τ_{it} from uncertainties in a and b for the linear fit (Appendix B).

Calculated threshold values and their uncertainties, illustrated in Figure 4a and listed in Table 1, are comparable to wind tunnel measured values of τ_{ft} (Bagnold, 1937; Chepil, 1945; Fletcher, 1976; Kok et al., 2012, Figure 5; Zingg, 1953) and τ_{it} (Bagnold, 1937; Chepil, 1945; Iversen & Rasmussen, 1994; B. Li & McKenna Neuman, 2012; Kok et al., 2012, Figure 21) for sediment bed grain sizes similar to those measured at our field sites. Models relating τ_{ft} (Bagnold, 1941; Iversen & White, 1982; Shao & Lu, 2000) and τ_{it} (Bagnold, 1941; Kok et al., 2012) to particle diameter, which generally align with these wind tunnel values (Kok et al., 2012), also correspond to our measured values for τ_{ft} and τ_{it} (Figure 5), lending support to our calculations.

4.2. Threshold Ratios

Converting fluid and impact threshold stresses to threshold shear velocities by equation (4), we calculate threshold ratios as

$$\frac{u_{*it}}{u_{*ft}} = \sqrt{\frac{\tau_{it}}{\tau_{ft}}}. \tag{9}$$

Based on equation (9), we calculate $u_{*,\,it}/u_{*,\,ft}$= 0.813 ± 0.018, 0.863 ± 0.027, and 0.837 ± 0.007 at Jericoacoara, Rancho Guadalupe, and Oceano, respectively (Table 1). These values are consistent with laboratory measurements (Bagnold, 1937; Chepil, 1945; Iversen & Rasmussen, 1994) and numerical predictions (Kok, 2010a) of $u_{*,\,it}/u_{*,\,ft} \approx 0.82$ (i.e., $\tau_{it}/\tau_{ft} \approx 0.67$). As with threshold stresses, we compute uncertainties in $u_{*,\,it}/u_{*,\,ft}$ by following standard error propagation methods (Appendix B).

5. Discussion

Our results build on the statistical TFEM (Stout & Zobeck, 1997) to provide the first field-based derivation of separate fluid and impact thresholds in aeolian saltation. Though fluid and impact thresholds for saltation initiation and cessation have long been theorized (e.g., Bagnold, 1937; Kok, 2010b) and measured in wind tunnel experiments (e.g., Chepil, 1945; Iversen & Rasmussen, 1994), the difficulty of directly measuring threshold crossings in the field (e.g., Barchyn & Hugenholtz, 2011) has limited the ability of past studies to resolve both thresholds. To overcome these limitations, we hypothesized, based on observations (Figure 1), that the relative contributions of fluid and impact thresholds in controlling saltation occurrence vary systematically with the frequency of saltation transport (equation (1)). As expected from this dual threshold hypothesis, we observed that the statistically defined effective threshold stress (Stout, 2004; Stout & Zobeck, 1997; Figure 2) decreases linearly with saltation activity between two end-member cases of fluid threshold dominance in the rare transport limit and impact threshold dominance in the continuous transport limit (Figure 4a). Based on these limiting effective threshold values, we then calculated distinct fluid and impact threshold stresses at the three field sites, which we found to be consistent with past theory and experiments.

Our observations offer two primary pieces of evidence supporting the combined role of distinctive fluid and impact thresholds in controlling saltation occurrence. First, a systematic decrease in effective threshold with increasing saltation activity (Figure 4a) is consistent with our dual threshold hypothesis (equation (1)), which predicts a gradual shift from fluid threshold to impact threshold control with increasing transport activity. Second, our estimated values for impact and fluid threshold (Table 1) are consistent with independent laboratory- and model-based estimates for both of these thresholds as a function of grain size (Figure 5). These pieces of evidence thus also lend support to our statistically based approach for determining fluid and impact thresholds from field measurements of wind speed and saltation activity.

5.1. Potential Limitations and Sensitivity Analyses

Despite this evidence supporting the existence of dual thresholds, we consider aspects of our methodology that could produce an artificial variation in effective threshold with saltation activity. First, our measured thresholds could depend on the selection of averaging intervals δt (Figure 2; Barchyn & Hugenholtz, 2011; Schönfeldt, 2003; Stout, 1998; Wiggs, Atherton, & Baird, 2004). Saltation is more likely to occur within longer δt increments (Figure 2b), thus increasing f_Q (Figure 2c; Sherman et al., 2017). Longer δt also decreases the amplitude of wind fluctuations (Figure 2e), which reduces the range of measured effective thresholds u_{th} (Figure 2f). To evaluate these δt effects, we perform a sensitivity analysis to reinvestigate the τ_{th} versus f_Q relationship for five values of δt ranging over 1–4 s, corresponding to typical saltation response time estimates (e.g., Anderson & Haff, 1988; Ma & Zheng, 2011; McEwan & Willetts, 1991). Figure 6a shows that the τ_{th} versus f_Q relationship is somewhat affected by variation in δt. In particular, increasing δt causes a decrease in τ_{it}, a slight increase in τ_{ft}, and thus a reduction in the threshold ratio $u_{*\mathrm{it}}/u_{*\mathrm{ft}}$ (Table 2). Nonetheless, for all δt between 1 and 4 s, calculated values of τ_{it}, τ_{ft}, and $u_{*\mathrm{it}}/u_{*\mathrm{ft}}$ remain broadly consistent with independent measurements (e.g., Bagnold, 1937; Kok, 2010b).

Second, our findings could also depend on the selection of analysis interval Δt, which partially determines the distribution of wind speeds Φ_u from which u_{th} values are calculated. In particular, we consider the possibility that our calculated u_{ft} and u_{it} values are merely statistical artifacts of our threshold determination method, arising simply from the respective lower and upper limits of the Φ_u distribution. If this were the case, increasing Δt, which typically produces a wider wind speed distribution Φ_u, would widen the separation between calculated τ_{ft} and τ_{it} values. However, sensitivity analyses for Δt= 0.5–30 min reveal no systematic trends (Figure 6b). This insensitivity to Δt leads us to reject the possibility that τ_{ft} and τ_{it} are merely statistical artifacts of our methodology. Such insensitivity to Δt also suggests that our adoption of the law of the wall and associated calculation of the roughness height for conversion from threshold wind speed to threshold shear velocity (equation (3)) is unaffected by measurement time interval (section 3.3).

Third, other factors, such as soil moisture (Davidson-Arnott et al., 2005, 2008; Stout, 2004; Wiggs, Baird, & Atherton, 2004) and turbulence properties (Davidson-Arnott et al., 2005; McKenna Neuman et al., 2000) could have contributed to observed threshold variations. To investigate these factors, we perform a sensitivity analysis by time of day, which we interpret as a proxy for changes in soil moisture and atmospheric stability. This sensitivity analysis shows no systematic trend of increasing or decreasing thresholds through the course of

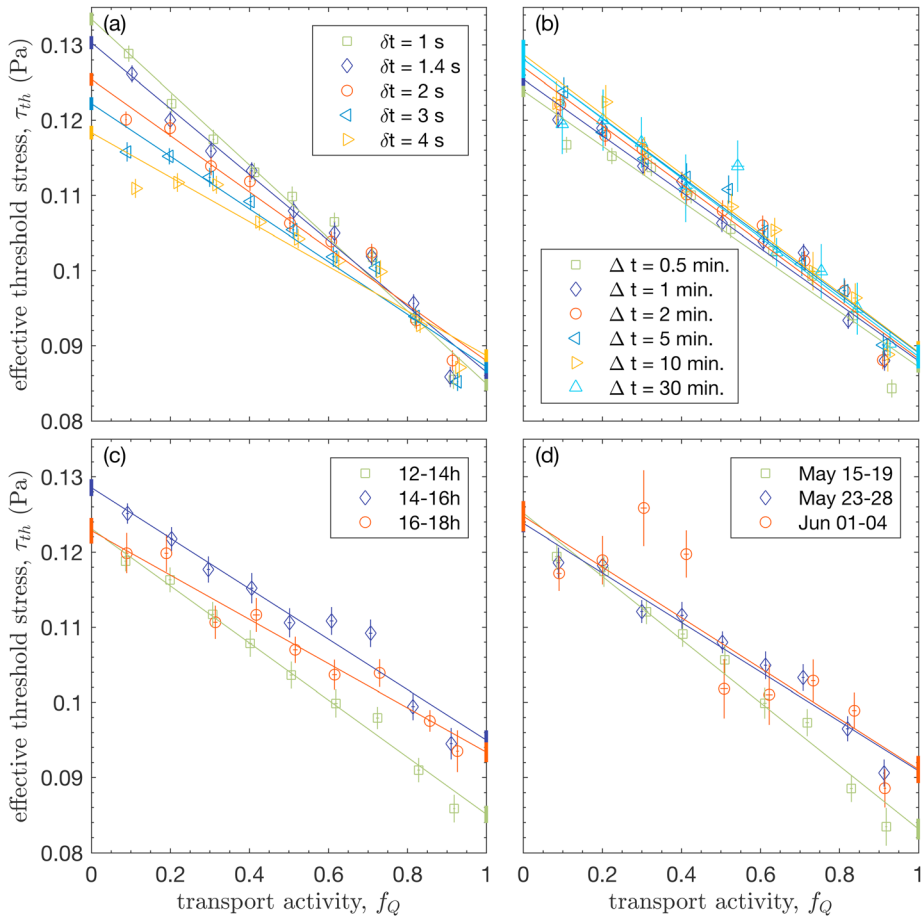

Figure 6. Sensitivity analyses comparing effective threshold τ_{th} and saltation transport activity f_Q. We limit our analyses here to the Oceano field site, where the most data are available to explore a wide range of averaging intervals δt, analysis intervals Δt, and conditional analyses by time of day and date. For all plots, limiting fluid and impact threshold values and their uncertainties, indicated by vertical bars at $f_Q = 0$ and $f_Q = 1$, respectively, are given in Table 2. (a) τ_{th} versus f_Q comparison for values of δt=1–4 s. Analysis interval Δt is fixed at 1 min for this analysis. (b) Comparison for six different analysis intervals Δt=0.5–30 min. Averaging interval δt is fixed at 2 s for this analysis. (c) Comparison for three different time periods for the diurnal cycle at Oceano. Here both averaging interval (δt = 2 s) and analysis interval (Δt = 1 min) are fixed. (d) Comparison for three date range segments of the deployment at Oceano, each of which is characterized by a distinctive surface grain size (Table 2) or wind speed (Figure 7) distribution. Again, δt and Δt are fixed.

the day (Figure 6c). Though the three diurnal periods do show some variation in limiting fluid and impact threshold values, a similar ratio of fluid and impact thresholds is maintained throughout the day. This analysis suggests the insensitivity of the thresholds measured at our field sites to soil moisture and turbulence factors. However, further work is needed to understand the sensitivity of thresholds to atmospheric stability (e.g., Frank & Kocurek, 1994) and soil moisture—especially at coastal sites subject to wide variations in moisture conditions (e.g., Davidson-Arnott et al., 2008).

Fourth, unexplained variation in grain size (Stout, 2007; Wiggs, Atherton, & Baird, 2004) could have also played a role in the observed variations in effective threshold. To investigate the effect of grain size, we perform a sensitivity analysis by date, which we interpret as a proxy for the coarsening of surface grain size distributions through time at the Oceano field site (Table 2). This analysis indeed indicates slight increases in thresholds during periods of coarser sediment sizes, consistent with expectations (Figure 6d). More generally, differences in grain size distributions do produce differences in effective thresholds among sites (Table 1), and these differences are consistent with expected impact and fluid thresholds (e.g., Kok et al., 2012) for the sand particle size distributions at each site. Such variations in thresholds with sand bed texture (e.g., Greeley & Iversen, 1985) merit further investigation in the future.

Table 2
Best Fit Values for Sensitivity Analyses at Oceano Field Site for Averaging Interval δt (Figure 6a), Analysis Interval Δt (Figure 6b), Diurnal Time Interval (Figure 6c), and Date Range (Figure 6d)

	Fluid threshold, τ_{ft} (Pa)	Impact threshold, τ_{it} (Pa)	Threshold ratio, $u_{*,\,it}/u_{*,\,ft}$
Averaging interval δt (s)	For sensitivity analysis (Figure 6a), Δt held constant at 1 min		
1	0.133 ± 0.001	0.085 ± 0.001	0.798 ± 0.008
1.4	0.130 ± 0.001	0.086 ± 0.001	0.815 ± 0.008
2	0.125 ± 0.001	0.088 ± 0.001	0.837 ± 0.007
3	0.122 ± 0.001	0.087 ± 0.001	0.844 ± 0.007
4	0.118 ± 0.001	0.089 ± 0.001	0.866 ± 0.007
Analysis interval Δt (min)	For sensitivity analysis (Figure 6b), δt held constant at 2 s		
0.5	0.124 ± 0.001	0.087 ± 0.001	0.839 ± 0.007
1	0.125 ± 0.001	0.088 ± 0.001	0.837 ± 0.007
2	0.127 ± 0.001	0.088 ± 0.001	0.833 ± 0.008
5	0.128 ± 0.001	0.089 ± 0.001	0.834 ± 0.010
10	0.129 ± 0.002	0.089 ± 0.001	0.832 ± 0.013
30	0.128 ± 0.003	0.089 ± 0.002	0.831 ± 0.016
Diurnal time interval	For sensitivity analysis (Figure 6c), δt and Δt held constant at 2 s and 1 min, respectively		
12–14 hr	0.123 ± 0.001	0.085 ± 0.001	0.831 ± 0.010
14–16 hr	0.129 ± 0.001	0.095 ± 0.001	0.859 ± 0.010
16–18 hr	0.123 ± 0.002	0.093 ± 0.001	0.872 ± 0.011
Date interval	For sensitivity analysis (Figure 6d), δt and Δt held constant at 2 s and 1 min, respectively		
15–19 May[a]	0.125 ± 0.001	0.083 ± 0.001	0.815 ± 0.012
23–28 May[b]	0.124 ± 0.001	0.091 ± 0.001	0.857 ± 0.010
1–4 June[c]	0.125 ± 0.002	0.091 ± 0.002	0.854 ± 0.015

Note. Uncertainties correspond to linear fitting uncertainty, which accounts for the uncertainty in the individual data points used for this fitting.
[a]Median, 10th percentile, and 90th percentile grain diameters of surface particles for this date interval are d_{50}= 0.346 ± 0.053 mm, d_{10}= 0.181 ± 0.017 mm, and d_{90}= 0.580 ± 0.061, respectively. [b]For this date interval, reference grain diameters are d_{50}=0.417 ± 0.056, d_{10}=0.193 ± 0.032, and d_{90}= 0.664 ± 0.051. [c]For this date interval, reference grain diameters are d_{50}= 0.415 ± 0.074, d_{10}= 0.194 ± 0.029, and d_{90}= 0.677 ± 0.079.

Fifth, it is also possible that the assumptions underlying our conversion from threshold wind speed to shear velocity (equation (3)) could bias our calculations. We assume that such conversion is possible for quasi-instantaneous wind measurements; however, Lee and Baas (2012) show that use of streamline-corrected wind values for shear stress calculations may introduce errors at short time scales. Lee and Baas (2016) further caution about uncertainties in short time scale estimates of shear stress arising from variability in turbulence structures. We also assume constant roughness height z_0 and thus neglect increasing momentum extraction by the saltation cloud with increasing saltation intensity (e.g., Sherman, 1992), which could further bias our calculations. By using z_0 instead of the larger z_s, we could be systematically underestimating $u_{*,\,th}$ in comparison to actual values. Error in the assumed saltation height could thus affect total saltation flux predictions (e.g., Rasmussen & Sørensen, 1999). It is also possible that the effective von Karman parameter decreases during saltation (B. Li et al., 2010), causing a further systematic underestimation in $u_{*,\,th}$. Despite all of these methodological issues associated with threshold stress calculations, which lack easy resolution, we reiterate the general robustness of our threshold results to variation in averaging and analysis intervals (Figure 6).

Sixth, differences in wind distributions, topography, sand bed characteristics, and instrument configurations may have produced additional unexplained variations in threshold values determined for different field sites. To explore the effect of wind distribution, we examine two distinctive intervals of dates at Oceano, 23–28 May and 1–4 June, for which surface grain size distributions were similar (Table 2) but horizontal wind speed distributions differed substantially (Figure 7). Despite wind distribution differences, the fluid and impact thresholds calculated over both of these date intervals are almost exactly the same. This is because the method of determining threshold depends only on the subset of time intervals for which saltation is intermittent, and the characteristics of the wind during such time intervals are likely independent of the overall wind distribution. Further understanding of how such site-specific factors affect threshold calculations would require additional measurements of site characteristics, which are beyond the scope of this work. However, as we explain in section 5.2 below, the threshold values obtained here agree with independently measured threshold values, within uncertainty ranges. Thus, we expect that the error bars on our threshold estimates roughly account for unexplained site-specific factors.

5.2. Interpretations of Dual Thresholds

Recent wind tunnel measurements support our interpretations of how fluid and impact thresholds govern saltation transport. Walter et al. (2014) found that so long as saltation activity is continuous (i.e., f_Q = 1), bed surface shear stress τ_0 remains constant with changes in Q. By Owen's hypothesis (Owen, 1964), Walter et al. interpreted this constant τ_0 as implying a constant rate of wind momentum dissipation at the bed surface equal to the impact threshold stress τ_{it}. However, they also observed τ_0 to decrease monotonically from τ_{ft} to τ_{it} during the transition from no saltation to continuous saltation (Figure 4 in Walter et al., 2014), suggesting that τ_0, like effective threshold τ_{th} (Figure 4a), is governed by changes in f_Q modulating the relative importance of fluid and impact thresholds. Paterna et al. (2016) further observed that transport initiation events during weak saltation are dominantly related to energetic turbulent eddies directly mobilizing particles from the bed surface (i.e., fluid entrainment). In contrast, as saltation strengthens, variations in saltation flux decouple from the occurrence of turbulence structures, as the splash process (i.e., impact entrainment) plays an increasing role in sustaining saltation and transporting momentum to the bed surface. These findings, that the processes governing wind momentum transfer (Paterna et al., 2016) and dissipation (Walter et al., 2014) display fluid threshold control during weak saltation and impact threshold control during

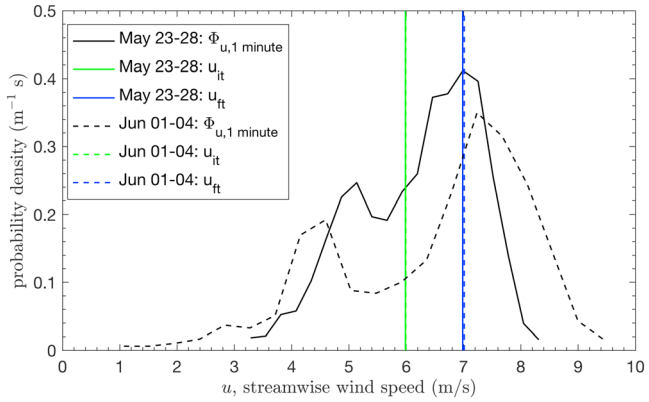

Figure 7. Wind speed distributions and associated thresholds for two sets of dates at the Oceano field site—23–28 May 2015 and 1–4 June 2015—both of which are characterized by similar surface grain size distributions (see Table 2). $\Phi_{u,\ 1\ minute}$ refers to the distribution of 1-min streamwise wind speeds during each date interval. u_{it} and u_{ft}, the respective impact and fluid threshold wind speeds for each date interval, are obtained by applying equations (3) and (4) to the respective threshold stresses for the date intervals (Figure 6d and Table 2).

intense saltation, are consistent with our dual threshold hypothesis (equation (1)) relating fluid to impact threshold contributions to the saltation activity.

Based on equation (1) and these recent wind tunnel studies, we expect impact threshold to dominate saltation dynamics in the limit of continuous (f_Q = 1) transport associated with moderate to strong saltation. We can gain insight into the importance of this continuous transport impact threshold control in saltation flux modeling by comparing fluid and impact threshold stresses calculated here to independent *flux-based* threshold stresses $\tau_{th,\ flux}$. These were obtained by Martin and Kok (2017) from the zero intercept of the linear fit to saltation flux Q versus shear stress τ, that is,

$$Q \propto \left(\tau - \tau_{th,flux}\right). \tag{10}$$

For all three sites, values for $\tau_{th,\ flux}$ agree with our τ_{it} measurements within 2σ uncertainty ranges, and $\tau_{th,\ flux}$ values are closer to τ_{it} than to τ_{ft} (Figure 4). We explain this general agreement between $\tau_{th,\ flux}$ and τ_{it} by the fact that most observed saltation at our field sites occurred under continuous or near-continuous transport conditions, for which τ_{it} dominantly controls wind momentum dissipation (Walter et al., 2014) and the zero intercept of the flux law (Martin & Kok, 2017). Compared to the range of τ/τ_{it} = ~1–4 over which saltation is observed at our field sites and those reported in the literature (Farrell et al., 2012; Greeley et al., 1996; B. Li et al., 2010; Namikas, 2003), the range of shear stresses for which saltation is intermittent (roughly τ/τ_{it} = 1 − 1.5, Figure 8) is relatively narrow. A new analytical model (Pähtz & Durán, 2018) posits the existence of a lower rebound and higher continuous rebound threshold, which together may control transitions among zero, partial, and continuous transport at stresses similar to our observed τ_{it} and τ_{ft}. Furthermore, saltation flux increases proportionately with τ/τ_{it} (Creyssels et al., 2009; Martin & Kok, 2017), which further weights the contribution of continuous transport conditions to the total volume of sand that is transported. Although the exact partitioning of sand flux between intermittent and continuous conditions is sensitive to the particular wind speed distribution for a specific field site and time period, a systematic study by Jerolmack and Brzinski (2010, Table 1) indicates that most transported sand is moved by $\tau/\tau_{it} \geq 1.5$ winds, for which we expect continuous saltation conditions governed by τ_{it}. Consequently, our results suggest that the importance of τ_{ft} is to serve as a rough boundary between intermittent and continuous saltation (Figure 8), whereas τ_{it} alone might serve as the de facto saltation threshold in studies modeling saltation flux over long time intervals (i.e., 30 min).

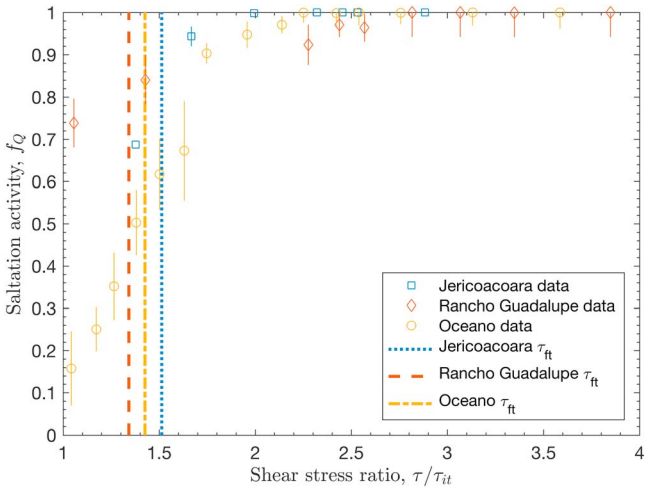

Figure 8. Saltation transport activity f_Q versus shear stress ratio τ/τ_{it}. Shear stress values are computed over 30-min intervals from the Reynolds stress (Martin & Kok, 2017), and corresponding f_Q values are combined into bins by range of τ. Error bars indicate standard error for each bin. Dashed lines indicate fluid threshold τ_{ft} at each site from Figure 4a.

5.3. Selection of Thresholds for Aeolian Saltation Flux and Dust Emission Modeling

Our findings offer insight into how thresholds should be incorporated into models for saltation occurrence, saltation flux, and dust emission. Both fluid and impact threshold should be used together when considering high-frequency saltation fluctuations, for which the flux-based threshold appears to be partially governed by averaging timescale (Martin et al., 2013). Dual thresholds should also be considered when intermittent saltation is the primary object of study (Baas & Sherman, 2005; Davidson-Arnott et al., 2012; Rasmussen & Sørensen, 1999; Sherman et al., 2017; Stout, 2004; Stout & Zobeck, 1997; Wiggs, Atherton, & Baird, 2004) or when modeling saltation on Mars (Kok, 2010b) or other planetary bodies (Pähtz & Durán, 2017) where the gap between fluid and impact thresholds is much larger than on Earth. However, when modeling saltation flux over longer analysis intervals (i.e., 30 min), such as in large-scale models for wind erosion (e.g., Shao & Leslie, 1997), dune migration (e.g., Fryberger et al., 1979), and dust emission (e.g., Gillette & Passi, 1988), our results indicate that use of the

impact threshold alone is sufficient, because most saltation occurs during periods of continuous transport (Figure 8). In fact, impact threshold is already widely used as the sole threshold value for saltation predictions (e.g., Andreotti, 2004; Ho et al., 2011; Sherman & Li, 2012; Ungar & Haff, 1987).

For the $\tau/\tau_{it} \approx 1 - 4$ range over which we observe saltation (Figure 8), the choice of impact versus fluid threshold for saltation modeling (i.e., by equation (10)) will produce at least a 10% difference in the prediction for saltation flux (and a >50% difference for $\tau/\tau_{it} < 2$). Therefore, adoption of the impact threshold, instead of the commonly used higher fluid threshold (e.g., Iversen & White, 1982; Marticorena & Bergametti, 1995; Shao, 2008), could improve predictions for saltation flux. Since the dust emission flux is generally modeled as proportional to the saltation flux (Kok et al., 2012; e.g., Marticorena & Bergametti, 1995; Shao, 2008), our findings have the potential to also improve predictions of dust emission fluxes.

Ideally, τ_{ft} and τ_{it} in saltation and dust modeling studies could be determined empirically by the methods we have described above, thus accounting for idiosyncratic variations in sand properties among sites (e.g., Webb et al., 2016). Otherwise, in cases where direct measurements of τ_{ft} and τ_{it} are not possible, such as on other planetary bodies (e.g., Pähtz & Durán, 2017), thresholds could be estimated from theoretical relationships (e.g., Claudin & Andreotti, 2006; Kok, 2010b), numerical models (e.g., Almeida et al., 2008; Kok, 2010a; Pähtz et al., 2012), or experimental studies (e.g., Chepil, 1945; Iversen & White, 1982), based on known median surface grain diameters and atmospheric properties. However, such estimates of threshold values and their effects on saltation occurrence may be complicated by uncertainties in measurements of wind speeds, turbulence properties, soil moisture, and sediment size distributions. In addition, translation of saltation activity and threshold values among different modes of investigation (i.e., observational, experimental, theoretical, and numerical) is fraught with issues of measurement scale and methodology (e.g., Barchyn, Martin, et al., 2014; Martin et al., 2013), leading to suggestions for standardized analysis protocols (Barchyn et al., 2011; Ellis et al., 2009; Sherman et al., 2017). Further work is needed to improve measurement techniques, standardize analysis protocols, and constrain the role of environmental factors in the determination of threshold values.

6. Conclusions

Applying the statistical TFEM (Stout & Zobeck, 1997) to high-frequency measurements of saltation and wind, here we provided the first field-based derivation of distinct fluid and impact thresholds for the respective initiation and cessation of aeolian saltation. The measured ratio of these thresholds is consistent with past laboratory and numerical studies of dual thresholds. We calculated fluid and impact thresholds by examining their roles in regulating saltation activity. When saltation is active a small fraction of the time, wind exceedance of fluid threshold controls saltation occurrence. As saltation activity increases, so too does the influence of the impact threshold, until saltation occurrence is controlled mostly by wind exceedance of impact threshold under near-continuous transport conditions. Although dual thresholds are thus required for certain saltation modeling applications, our results indicate that the impact threshold alone is sufficient for predicting the time-averaged (~30-min) saltation flux on Earth. Consequently, we suggest that parameterizations of sand and dust transport in aeolian process models can simply adopt the impact threshold for most predictions.

Appendix A: Accounting for False Negatives in Calculation of Saltation Activity

Here we derive a method to account for the possibility of *false negatives* (i.e., instances in which saltation transport occurs but is not detected) when computing saltation activity f_Q. To do so, we distinguish the measured saltation detection rate f_D from the actual saltation activity f_Q. We compute f_D as the fraction of averaging intervals δt in each analysis interval Δt for which total particle counts rate N is nonzero. We then estimate f_Q from f_D by calculating the expected rate of false negatives for particle arrivals occurring as a Poisson counting process. We detail this procedure below.

By Bayes' theorem, we have

$$f_{D|Q} = \frac{f_D f_{Q|D}}{f_Q}, \tag{A1}$$

where $f_{D\ |\ Q}$ is the conditional probability of detecting transport when it is active, and $f_{Q\ |\ D}$ is the probability that transport is actually active when it has been detected. We observed that the Wenglor optical particle counters did not produce *false positives*, that is, that detection necessarily implied transport and therefore

that $f_{Q\mid D} = 1$. However, we found that during conditions of weak transport or few Wenglor counters, false negatives could occur with some regularity due to the limited sampling volume of individual counters. Denoting these false negatives as $f_{\sim D\mid Q}$ and noting that $f_{\sim D\mid Q} + f_{D\mid Q} = 1$, we can restate equation (A1) as

$$f_Q = \frac{f_D}{1 - f_{\sim D|Q}}. \tag{A2}$$

To estimate the rate of false negatives $f_{\sim D\mid Q}$, we treat particle arrivals as a Poisson counting process. For such a process

$$f_{\sim D|Q} = \exp(-\lambda), \tag{A3}$$

where λ is the average arrival rate of particles per δt averaging interval at times when transport is active. We calculate λ as

$$\lambda = \overline{N}\delta t/f_D, \tag{A4}$$

where $\overline{N}$ is the mean particle counts rate during the analysis interval Δt = 1 min. Combining equations (A2)–(A4), we have

$$f_Q = \frac{f_D}{1 - \exp(-\lambda)} = \frac{f_D}{1 - \exp\left(-\overline{N}\delta t/f_D\right)}. \tag{A5}$$

The effect of the false negative correction in computing f_Q can be seen in supporting information Figure S2. During strong transport, λ is large so $f_Q \approx f_D$ in equation (A5). However, when transport is weak, δt is small, or the number of Wenglors are few, λ can be much smaller than 1, and therefore the correction causes f_Q to significantly exceed f_D.

Appendix B: Estimation of Uncertainties for Effective Threshold Wind Speeds, Shear Velocities, and Shear Stresses

To facilitate uncertainty estimation for computed effective thresholds, we combine effective threshold wind speed values u_{th} from individual Δt analysis intervals into bins defined by ranges of flux activity f_Q. For each bin, we compute bin-averaged threshold and activity values for u_{th} and f_Q, then we calculate their uncertainties from the standard errors of values in each bin. When converting each bin-averaged effective threshold wind speed u_{th} to an effective threshold shear velocity $u_{*,\,\mathrm{th}}$ and shear stress τ_{th}, we perform error propagation to estimate uncertainties in $u_{*,\,\mathrm{th}}$ and τ_{th}.

For each site, we group values of u_{th} for individual Δt together into bins covering ranges of f_Q. To accommodate the uneven spread of data points across the range of possible f_Q, we allow for creation of bins covering varying ranges of f_Q. We establish these criteria to balance the need for a sufficient number of data points in each bin with the need to limit the maximum width of the bins. The procedure for generating the binned values for each site is as follows:

1. Sort all u_{th} data points in order of increasing f_Q. Because the effective threshold calculation (equation (2)) assumes intermittent transport conditions, exclude data points with $f_Q < 0.05$ and $f_Q > 0.95$.
2. Starting from the lowest remaining f_Q, add data points to the bin, until the following criteria are achieved for the bin

a $\max(f_Q) - \min(f_Q) \geq 0.1$ (minimum bin width), *and*
b There are at least three points in the bin *or* $\max(f_Q) - \min(f_Q) > 0.2$ (maximum bin width).

3. Once the bin is full, repeat step 2 for the next bin.

For each bin i, we determine the mean value for flux activity $f_{Q,\,i}$ and its uncertainty $\sigma_{f_{Q,i}}$ as

$$f_{Q,i} = \sum\nolimits_j f_{Q,j}/N_i, \tag{B1}$$

$$\sigma_{f_{Q,i}} = \frac{\sqrt{\sum_j \left(f_{Q,j} - f_{Q,i}\right)^2}}{\sqrt{N_i}}, \tag{B2}$$

where $f_{Q,\,j}$ are the individual values of flux activity in the bin and N_i is the total number of values in the bin. Equation (B2) is computed based on the typical formulation for the standard error (equation 4.14 in

Bevington & Robinson, 2003). Similarly, the mean effective threshold wind speed $u_{\mathrm{th},\,i}$ and its uncertainty $\sigma_{u_{\mathrm{th},i}}$ are

$$u_{\mathrm{th},i} = \sum\nolimits_j u_{\mathrm{th},j}/N_i, \tag{B3}$$

$$\sigma_{u_{\mathrm{th},i}} = \frac{\sqrt{\sum_j \left(u_{\mathrm{th},j} - u_{\mathrm{th},i}\right)^2}}{\sqrt{N_i}}, \tag{B4}$$

where $u_{\mathrm{th},\,j}$ are the individual values of effective threshold in the bin.

We convert binned values for effective threshold wind speed $u_{\mathrm{th},\,i}$ to effective threshold shear velocity $u_{*,\,\mathrm{th}}$ by equation (3) and to effective threshold stress τ_{th} by equation (4). Using the error propagation formula (equation 3.14 in Bevington & Robinson, 2003), we propagate effective threshold wind speed uncertainty $\sigma_{u_{\mathrm{th}}}$ and roughness height uncertainty $\sigma_{\ln(z_0)}$ to derive uncertainty in threshold shear velocity $\sigma_{u_{*,\mathrm{th}}}$ and threshold stress $\sigma_{\tau_{\mathrm{th}}}$:

$$\sigma_{u_{*,\mathrm{th}}} = \frac{u_{*,\mathrm{th}}}{u_{\mathrm{th}}}\sqrt{\sigma_{u_{\mathrm{th}}}^2 + \frac{\ln^2(\sigma_{z_0})}{\ln^2(z_U/z_0)}u_{*,\mathrm{th}}^2}, \tag{B5}$$

$$\sigma_{\tau_{\mathrm{th}}} = 2\rho_f u_{*,\mathrm{th}}\sigma_{u_{*,\mathrm{th}}}. \tag{B6}$$

To determine uncertainties in fluid τ_{ft} and impact τ_{it} threshold stresses (equations (7) and (8)), we propagate uncertainties in the fitting intercept a and fitting slope b:

$$\sigma_{\tau_{\mathrm{ft}}} = \sigma_a, \tag{B7}$$

$$\sigma_{\tau_{\mathrm{it}}} = \sqrt{\sigma_a^2 + \sigma_b^2 + 2\sigma_{ab}^2} \tag{B8}$$

where σ_a and σ_b are the respective uncertainties in a and b, and σ_{ab}^2 is their covariance. We then apply error propagation to the threshold ratio $u_{*\mathrm{it}}/u_{*\mathrm{ft}}$ to calculate its uncertainty:

$$\sigma_{u_{*\mathrm{it}}/u_{*\mathrm{ft}}} = \frac{1}{2}\sqrt{\frac{\sigma_{\tau_{\mathrm{it}}}^2}{\tau_{\mathrm{it}}\tau_{\mathrm{ft}}} + \frac{\sigma_{\tau_{\mathrm{ft}}}^2\tau_{\mathrm{it}}}{\sigma_{\tau_{\mathrm{ft}}}^3}}. \tag{B9}$$

Appendix C: List of Variables

Below we list all variables described in the manuscript. Typical units for variables are given in parentheses, if applicable.

- u_* = shear velocity (m/s)
- $u_{*\mathrm{ft}}$ = fluid threshold shear velocity (m/s)
- $u_{*\mathrm{it}}$ = impact threshold shear velocity (m/s)
- $u_{*\mathrm{it}}/u_{*\mathrm{ft}}$ = shear velocity threshold ratio
- $u_{*,\,\mathrm{th}}$ = effective threshold shear velocity (m/s)
- $u_{*,\,Re}$ = Reynolds stress-based shear velocity (m/s)
- τ = wind shear stress (Pa)
- τ_{ft} = fluid threshold shear stress (Pa)
- τ_{it} = impact threshold shear stress (Pa)
- τ_{th} = effective threshold shear stress (Pa)
- f_Q = saltation transport activity; that is, fraction of time saltation is active
- $u(t)$ = time series of horizontal wind speed (m/s)
- z_U = anemometer height above the sand surface (m)
- u_{ft} = fluid threshold wind speed (m/s)
- u_{it} = impact threshold wind speed (m/s)
- u_{th} = effective threshold wind speed (m/s)
- d_{50} = median diameter of surface particles by volume (mm)
- d_{10} = 10th percentile diameter of surface particles by volume (mm)
- d_{90} = 90th percentile diameter of surface particles by volume (mm)

N = vertically integrated saltation particle counts rate (counts/s)
δt = averaging time interval (s)
Δt = analysis time interval (min)
Φ_u = cumulative distribution of δt streamwise wind speeds u
$\Phi_{u,\ 1\ \mathrm{minute}}$ = distribution of 1-min streamwise wind speeds
κ = von Karman parameter
z_0 = aerodynamic roughness height (m)
$\sigma_{\ln(z_0)}$ = natural log uncertainty in aerodynamic roughness height
z_s = effective roughness height, accounting for saltation-induced roughness (m)
ρ_f = air density (kg/m^3)
θ = angle of horizontal wind relative to dominant sand-transporting wind
$|z/L|$ = stability parameter
Q = saltation flux (g/m/s)
a = least squares linear fitting intercept
b = least squares linear fitting slope
τ_0 = bed surface shear stress (Pa)
$\tau_{\mathrm{th,\ flux}}$ = flux-based estimate of threshold stress (Pa)
f_D = saltation detection rate
$f_{Q\ |\ D}$ = probability that transport is actually active when it has been detected
$f_{D\ |\ Q}$ = conditional probability of detecting transport when it is active
$f_{\sim D\ |\ Q}$ = conditional probability of not detecting transport when it is active
λ = average arrival rate of particles (counts/s)
$\overline{N}$ = mean vertically integrated saltation particle counts rate (counts/s)
$f_{Q,\ i}$ = mean value for saltation transport activity for bin i
$\sigma_{f_{Q,i}}$ = uncertainty in saltation transport activity for bin i
$f_{Q,\ j}$ = individual values j of saltation activity in bin i
N_i = number of values in bin i
$u_{\mathrm{th},\ i}$ = mean value for effective threshold wind speed for bin i (m/s)
$\sigma_{u_{\mathrm{th},i}}$ = uncertainty in effective threshold wind speed for bin i (m/s)
$u_{\mathrm{th},\ j}$ = individual values j of effective threshold wind speed in bin i (m/s)
$\sigma_{u_{*,\mathrm{th}}}$ = uncertainty in effective threshold shear velocity (m/s)
$\sigma_{\tau_{\mathrm{th}}}$ = uncertainty in effective threshold shear stress (Pa)
σ_a = uncertainty of linear fitting intercept
σ_b = uncertainty of linear fitting slope
σ^2_{ab} = covariance of fitting slope and intercept
$\sigma_{\tau_{\mathrm{ft}}}$ = uncertainty in fluid threshold stress (Pa)
$\sigma_{\tau_{\mathrm{it}}}$ = uncertainty in impact threshold stress (Pa)
$\sigma_{u_{*\mathrm{it}}/u_{*\mathrm{ft}}}$ = uncertainty in shear velocity threshold ratio

Acknowledgments
U.S. National Science Foundation (NSF) Postdoctoral Fellowship EAR-1249918 to R. L. M. and NSF grant AGS-1358621 to J. F. K. supported this research. Research was also sponsored by the Army Research Laboratory and was accomplished under grant W911NF-15-1-0417. The views and conclusions contained in this document are those of the authors and should not be interpreted as representing the official policies, either expressed or implied, of the Army Research Laboratory or the U.S. Government. The U.S. Government is authorized to reproduce and distribute reprints for Government purposes notwithstanding any copyright notation herein. Oceano Dunes State Vehicular Recreation Area, Rancho Guadalupe Dunes Preserve, and Jericoacoara National Park provided essential site access and support. Jericoacoara fieldwork is registered with the Brazilian Ministry of the Environment (46254-1 to J. Ellis). We thank Marcelo Chamecki for advice on treatment of wind data; Chris Hugenholtz and Tom Barchyn for equipment help; Doug Jerolmack for lab access for grain size analysis; and Jean Ellis, Paulo Sousa, Peter Li, Francis Turney, Arkayan Samaddar, and Livia Freire for field assistance. We also thank M. Bayani Cardenas, Giovanni Coco, Doug Sherman, Cheryl McKenna Neuman, and seven anonymous reviewers for their thoughtful suggestions on several versions of this manuscript. Data included in the analysis for this paper can be found in supporting information Data Set S1 and on the Zenodo data repository at http://doi.org/10.5281/zenodo.574896.

References

Almeida, M. P., Parteli, E. J. R., Andrade, J. S., & Herrmann, H. J. (2008). Giant saltation on Mars. *Proceedings of the National Academy of Sciences of the United States of America*, *105*(17), 6222–6226. https://doi.org/10.1073/pnas.0800202105

Anderson, R. S., & Haff, P. K. (1988). Simulation of eolian saltation. *Science*, *241*(4867), 820–823. https://doi.org/10.1126/science.241.4867.820

Andreotti, B. (2004). A two-species model of aeolian sand transport. *Journal of Fluid Mechanics*, *510*, 47–70. https://doi.org/10.1017/S0022112004009073

Ayoub, F., Avouac, J.-P., Newman, C. E., Richardson, M. I., Lucas, A., Leprince, S., & Bridges, N. T. (2014). Threshold for sand mobility on Mars calibrated from seasonal variations of sand flux. *Nature Communications*, *5*(1), 5096. https://doi.org/10.1038/ncomms6096

Baas, A. C. W. (2008). Challenges in aeolian geomorphology: Investigating aeolian streamers. *Geomorphology*, *93*(1-2), 3–16. https://doi.org/10.1016/j.geomorph.2006.12.015

Baas, A. C. W., & Sherman, D. J. (2005). Formation and behavior of aeolian streamers. *Journal of Geophysical Research*, *110*, F03011. https://doi.org/10.1029/2004JF000270

Bagnold, R. A. (1937). The transport of sand by wind. *The Geographical Journal*, *89*(5), 409–438. https://doi.org/10.2307/1786411

Bagnold, R. A. (1941). *The physics of blown sand and desert dunes*. London: Dover.

Barchyn, T. E., & Hugenholtz, C. H. (2011). Comparison of four methods to calculate aeolian sediment transport threshold from field data: Implications for transport prediction and discussion of method evolution. *Geomorphology*, *129*(3-4), 190–203. https://doi.org/10.1016/j.geomorph.2011.01.022

Barchyn, T. E., Hugenholtz, C. H., & Ellis, J. T. (2011). A call for standardization of aeolian process measurements: Moving beyond relative case studies. *Earth Surface Processes and Landforms*, *36*(5), 702–705. https://doi.org/10.1002/esp.2136

Barchyn, T. E., Hugenholtz, C. H., Li, B., McKenna Neuman, C., & Sanderson, R. S. (2014). From particle counts to flux: Wind tunnel testing and calibration of the "Wenglor" aeolian sediment transport sensor. *Aeolian Research*, *15*, 311–318. https://doi.org/10.1016/j.aeolia.2014.06.009

Barchyn, T. E., Martin, R. L., Kok, J. F., & Hugenholtz, C. H. (2014). Fundamental mismatches between measurements and models in aeolian sediment transport prediction: The role of small-scale variability. *Aeolian Research*, *15*, 245–251. https://doi.org/10.1016/j.aeolia.2014.07.002

Bauer, B. O., & Davidson-Arnott, R. G. D. (2014). Aeolian particle flux profiles and transport unsteadiness. *Journal of Geophysical Research: Earth Surface*, *119*, 1542–1563. https://doi.org/10.1002/2014JF003128

Bevington, P. R., & Robinson, D. K. (2003). *Data reduction and error analysis for the physical sciences* (3rd ed.). New York: McGraw-Hill.

Bridges, N. T., Ayoub, F., Avouac, J.-P., Leprince, S., Lucas, A., & Mattson, S. (2012). Earth-like sand fluxes on Mars. *Nature*, *485*(7398), 339–342. https://doi.org/10.1038/nature11022

Carneiro, M. V., Rasmussen, K. R., & Herrmann, H. J. (2015). Bursts in discontinuous Aeolian saltation. *Scientific Reports*, *5*(1). https://doi.org/10.1038/srep11109

Chepil, W. S. (1945). Dynamics of wind erosion. 2. Initiation of soil movement. *Soil Science*, *60*, 397. https://doi.org/10.1097/00010694-194511000-00005

Claudin, P., & Andreotti, B. (2006). A scaling law for aeolian dunes on Mars, Venus, Earth, and for subaqueous ripples. *Earth and Planetary Science Letters*, *252*(1-2), 30–44. https://doi.org/10.1016/j.epsl.2006.09.004

Creyssels, M., Dupont, P., El Moctar, A. O., Valance, A., Cantat, I., Jenkins, J. T., et al. (2009). Saltating particles in a turbulent boundary layer: Experiment and theory. *Journal of Fluid Mechanics*, *625*, 47–74. https://doi.org/10.1017/S0022112008005491

Davidson-Arnott, R. G. D., & Bauer, B. O. (2009). Aeolian sediment transport on a beach: Thresholds, intermittency, and high frequency variability. *Geomorphology, Contemporary research in aeolian geomorphology 6th International Conference on Aeolian Research (ICAR VI)*, *105*, 117–126. https://doi.org/10.1016/j.geomorph.2008.02.018

Davidson-Arnott, R. G. D., Bauer, B. O., Walker, I. J., Hesp, P. A., Ollerhead, J., & Chapman, C. (2012). High-frequency sediment transport responses on a vegetated foredune. *Earth Surface Processes and Landforms*, *37*(11), 1227–1241. https://doi.org/10.1002/esp.3275

Davidson-Arnott, R. G. D., MacQuarrie, K., & Aagaard, T. (2005). The effect of wind gusts, moisture content and fetch length on sand transport on a beach. *Geomorphology*, *68*(1-2), 115–129. https://doi.org/10.1016/j.geomorph.2004.04.008

Davidson-Arnott, R. G. D., Yang, Y., Ollerhead, J., Hesp, P. A., & Walker, I. J. (2008). The effects of surface moisture on aeolian sediment transport threshold and mass flux on a beach. *Earth Surface Processes and Landforms*, *33*(1), 55–74. https://doi.org/10.1002/esp.1527

Durán, O., Claudin, P., & Andreotti, B. (2011). On aeolian transport: Grain-scale interactions, dynamical mechanisms and scaling laws. *Aeolian Research*, *3*(3), 243–270. https://doi.org/10.1016/j.aeolia.2011.07.006

Ellis, J. T., Li, B., Farrell, E. J., & Sherman, D. J. (2009). Protocols for characterizing aeolian mass-flux profiles. *Aeolian Research*, *1*(1-2), 19–26. https://doi.org/10.1016/j.aeolia.2009.02.001

Farrell, E. J., Sherman, D. J., Ellis, J. T., & Li, B. (2012). Vertical distribution of grain size for wind blown sand. *Aeolian Research*, *7*, 51–61. https://doi.org/10.1016/j.aeolia.2012.03.003

Fletcher, B. (1976). The incipient motion of granular materials. *Journal of Physics D*, *9*(17), 2471–2478. https://doi.org/10.1088/0022-3727/9/17/007

Frank, A., & Kocurek, G. (1994). Effects of atmospheric conditions on wind profiles and aeolian sand transport with an example from White Sands National Monument. *Earth Surface Processes and Landforms*, *19*(8), 735–745. https://doi.org/10.1002/esp.3290190806

Fryberger, S. G., Dean, G., & McKee, E. D. (1979). Dune forms and wind regime. In E. D. McKee (Ed.), *A study of global sand seas* (pp. 137–170). Washington, DC: U.S. Geological Survey Professional Paper 1052.

Gillette, D. A., & Passi, R. (1988). Modeling dust emission caused by wind erosion. *Journal of Geophysical Research*, *93*(D11), 14,233–14,242. https://doi.org/10.1029/JD093iD11p14233

Greeley, R., Blumberg, D. G., & Williams, S. H. (1996). Field measurements of the flux and speed of wind-blown sand. *Sedimentology*, *43*(1), 41–52. https://doi.org/10.1111/j.1365-3091.1996.tb01458.x

Greeley, R., & Iversen, J. D. (1985). *Wind as a geological process on Earth, Mars, Venus and Titan*. New York: Cambridge University Press.

Guala, M., Metzger, M., & McKeon, B. J. (2011). Interactions within the turbulent boundary layer at high Reynolds number. *Journal of Fluid Mechanics*, *666*, 573–604. https://doi.org/10.1017/S0022112010004544

Hilton, M., Nickling, B., Wakes, S., Sherman, D., Konlechner, T., Jermy, M., & Geoghegan, P. (2017). An efficient, self-orienting, vertical-array, sand trap. *Aeolian Research*, *25*, 11–21. https://doi.org/10.1016/j.aeolia.2017.01.003

Ho, T. D., Valance, A., Dupont, P., & Ould El Moctar, A. (2011). Scaling laws in aeolian sand transport. *Physical Review Letters*, *106*(9), 94,501. https://doi.org/10.1103/PhysRevLett.106.094501

Hugenholtz, C. H., & Barchyn, T. E. (2011). Laboratory and field performance of a laser particle counter for measuring aeolian sand transport. *Journal of Geophysical Research*, *116*, F01010. https://doi.org/10.1029/2010JF001822

Iversen, J. D., & Rasmussen, K. R. (1994). The effect of surface slope on saltation threshold. *Sedimentology*, *41*(4), 721–728. https://doi.org/10.1111/j.1365-3091.1994.tb01419.x

Iversen, J. D., & White, B. R. (1982). Saltation threshold on Earth, Mars and Venus. *Sedimentology*, *29*(1), 111–119. https://doi.org/10.1111/j.1365-3091.1982.tb01713.x

Jerolmack, D. J., & Brzinski, T. A. (2010). Equivalence of abrupt grain-size transitions in alluvial rivers and eolian sand seas: A hypothesis. *Geology*, *38*(8), 719–722. https://doi.org/10.1130/G30922.1

Jerolmack, D. J., Reitz, M. D., & Martin, R. L. (2011). Sorting out abrasion in a gypsum dune field. *Journal of Geophysical Research*, *116*, F02003. https://doi.org/10.1029/2010JF001821

Kok, J. F. (2010a). An improved parameterization of wind-blown sand flux on Mars that includes the effect of hysteresis. *Geophysical Research Letters*, *37*, L12202. https://doi.org/10.1029/2010GL043646

Kok, J. F. (2010b). Difference in the wind speeds required for initiation versus continuation of sand transport on Mars: Implications for dunes and dust storms. *Physical Review Letters*, *104*(7), 74502. https://doi.org/10.1103/PhysRevLett.104.074502

Kok, J. F., Mahowald, N. M., Fratini, G., Gillies, J. A., Ishizuka, M., Leys, J. F., et al. (2014). An improved dust emission model—Part 1: Model description and comparison against measurements. *Atmospheric Chemistry and Physics*, *14*(23), 13,023–13,041. https://doi.org/10.5194/acp-14-13023-2014

Kok, J. F., Parteli, E. J. R., Michaels, T. I., & Karam, D. B. (2012). The physics of wind-blown sand and dust. *Reports on Progress in Physics*, *75*(10), 106901. https://doi.org/10.1088/0034-4885/75/10/106901

Lee, Z. S., & Baas, A. C. W. (2012). Streamline correction for the analysis of boundary layer turbulence. *Geomorphology*, *171–172*, 69–82. https://doi.org/10.1016/j.geomorph.2012.05.005
Lee, Z. S., & Baas, A. C. W. (2016). Variable and conflicting shear stress estimates inside a boundary layer with sediment transport. *Earth Surface Processes and Landforms*, *41*(4), 435–445. https://doi.org/10.1002/esp.3829
Li, B., & McKenna Neuman, C. (2012). Boundary-layer turbulence characteristics during aeolian saltation. *Geophysical Research Letters*, *39*, L11402. https://doi.org/10.1029/2012GL052234
Li, B., Sherman, D. J., Farrell, E. J., & Ellis, J. T. (2010). Variability of the apparent von Karman parameter during aeolian saltation. *Geophysical Research Letters*, *37*, L15404. https://doi.org/10.1029/2010GL044068
Li, Z., Zhao, X., & Huang, W. (2008). A stochastic model for initial movement of sand grains by wind. *Earth Surface Processes and Landforms*, *33*, 1796–1803. https://doi.org/10.1002/esp.1638
Lindhorst, S., & Betzler, C. (2016). The climate-archive dune: Sedimentary record of annual wind intensity. *Geology*, *44*(9), 711–714. https://doi.org/10.1130/G38093.1
Lorenz, R. D., & Zimbelman, J. R. (2014). *Dune worlds*. Heidelberg: Springer.
Ma, G. S., & Zheng, X. J. (2011). The fluctuation property of blown sand particles and the wind-sand flow evolution studied by numerical method. *European Physical Journal E: Soft Matter and Biological Physics*, *34*(5), 34. https://doi.org/10.1140/epje/i2011-11054-3
Marticorena, B., & Bergametti, G. (1995). Modeling the atmospheric dust cycle: 1. Design of a soil-derived dust emission scheme. *Journal of Geophysical Research*, *100*(D8), 16,415–16,430. https://doi.org/10.1029/95JD00690
Martin, R. L., Barchyn, T. E., Hugenholtz, C. H., & Jerolmack, D. J. (2013). Timescale dependence of aeolian sand flux observations under atmospheric turbulence. *Journal of Geophysical Research: Atmospheres*, *118*, 9078–9092. https://doi.org/10.1002/jgrd.50687
Martin, R. L., & Kok, J. F. (2017). Wind-invariant saltation heights imply linear scaling of aeolian saltation flux with shear stress. *Science Advances*, *3*(6), e1602569. https://doi.org/10.1126/sciadv.1602569
Martin, R. L., Kok, J. F., Hugenholtz, C. H., Barchyn, T. E., Chamecki, M., & Ellis, J. T. (2018). High-frequency measurements of aeolian saltation flux: Field-based methodology and applications. *Aeolian Research*, *30*, 97–114. https://doi.org/10.1016/j.aeolia.2017.12.003
Marusic, I., Mathis, R., & Hutchins, N. (2010). Predictive model for wall-bounded turbulent flow. *Science*, *329*(5988), 193–196. https://doi.org/10.1126/science.1188765
McEwan, I. K., & Willetts, B. B. (1991). Numerical model of the saltation cloud. *Acta Mechanica Supplementa*, *1*, 53–66. https://doi.org/10.1007/978-3-7091-6706-9_3
McKenna Neuman, C., Lancaster, N., & Nickling, W. G. (2000). The effect of unsteady winds on sediment transport on the stoss slope of a transverse dune, Silver Peak, NV, USA. *Sedimentology*, *47*(1), 211. https://doi.org/10.1046/j.1365-3091.2000.00289.x
Namikas, S. L. (2003). Field measurement and numerical modelling of aeolian mass flux distributions on a sandy beach. *Sedimentology*, *50*(2), 303–326. https://doi.org/10.1046/j.1365-3091.2003.00556.x
Namikas, S. L., Bauer, B. O., & Sherman, D. J. (2003). Influence of averaging interval on shear velocity estimates for aeolian transport modeling. *Geomorphology*, *53*(3-4), 235–246. https://doi.org/10.1016/S0169-555X(02)00314-8
Nickling, W. G. (1988). The initiation of particle movement by wind. *Sedimentology*, *35*(3), 499–511. https://doi.org/10.1111/j.1365-3091.1988.tb01000.x
Nikuradse, J. (1933). *Laws of flow in rough pipes (1950 translation) (Tech. Memo. No. 1292)*. Washington, DC: National Advisory Committee for Aeronautics.
Owen, P. R. (1964). Saltation of uniform grains in air. *Journal of Fluid Mechanics*, *20*(02), 225–242. https://doi.org/10.1017/S0022112064001173
Pähtz, T., & Durán, O. (2017). Fluid forces or impacts, what governs the entrainment of soil particles in sediment transport mediated by a Newtonian fluid? *Physical Review Fluids*, *2*(7), 74303. https://doi.org/10.1103/PhysRevFluids.2.074303
Pähtz, T., & Durán, O. (2018). The cessation threshold of non-suspended sediment transport across environments. *Journal of Geophysical Research: Earth Surface*, 123. https://doi.org/10.1029/2017JF004580
Pähtz, T., Kok, J. F., & Herrmann, H. J. (2012). The apparent roughness of a sand surface blown by wind from an analytical model of saltation. *New Journal of Physics*, *14*(4), 43,035. https://doi.org/10.1088/1367-2630/14/4/043035
Paterna, E., Crivelli, P., & Lehning, M. (2016). Decoupling of mass flux and turbulent wind fluctuations in drifting snow. *Geophysical Research Letters*, *43*, 4441–4447. https://doi.org/10.1002/2016GL068171
Rasmussen, K. R., & Sørensen, M. (1999). Aeolian mass transport near the saltation threshold. *Earth Surface Processes and Landforms*, *24*(5), 413–422. https://doi.org/10.1002/(SICI)1096-9837(199905)24:5<413::AID-ESP997>3.0.CO;2-I
Rice, M. A., McEwan, I. K., & Mullins, C. E. (1999). A conceptual model of wind erosion of soil surfaces by saltating particles. *Earth Surface Processes and Landforms*, *24*, 383–392. https://doi.org/10.1002/(SICI)1096-9837(199905)24:5<383::AID-ESP995>3.0.CO;2-K
Salesky, S. T., Chamecki, M., & Dias, N. L. (2012). Estimating the random error in eddy-covariance based fluxes and other turbulence statistics: The filtering method. *Boundary-Layer Meteorology*, *144*(1), 113–135. https://doi.org/10.1007/s10546-012-9710-0
Schönfeldt, H. J. (2003). Remarks on the definition and estimation of the aeolian erosion threshold friction velocity. *Meteorologische Zeitschrift*, *12*(3), 137–142. https://doi.org/10.1127/0941-2948/2003/0012-0137
Schönfeldt, H. J. (2004). Establishing the threshold for intermittent aeolian sediment transport. *Meteorologische Zeitschrift*, *13*(5), 437–444. https://doi.org/10.1127/0941-2948/2004/0013-0437
Shao, Y. (2008). *Physics and modelling of wind erosion*. Netherlands: Springer.
Shao, Y., & Leslie, L. M. (1997). Wind erosion prediction over the Australian continent. *Journal of Geophysical Research*, *102*(D25), 30,091–30,105. https://doi.org/10.1029/97JD02298
Shao, Y., & Lu, H. (2000). A simple expression for wind erosion threshold friction velocity. *Journal of Geophysical Research*, *105*(D17), 22,437–22,443. https://doi.org/10.1029/2000JD900304
Sherman, D. J. (1992). An equilibrium relationship for shear velocity and apparent roughness length in aeolian saltation. *Geomorphology*, *5*(3-5), 419–431. https://doi.org/10.1016/0169-555X(92)90016-H
Sherman, D. J., & Li, B. (2012). Predicting aeolian sand transport rates: A reevaluation of models. *Aeolian Research*, *3*(4), 371–378. https://doi.org/10.1016/j.aeolia.2011.06.002
Sherman, D. J., Li, B., Ellis, J. T., Farrell, E. J., Maia, L. P., & Granja, H. (2013). Recalibrating aeolian sand transport models. *Earth Surface Processes and Landforms*, *38*(2), 169–178. https://doi.org/10.1002/esp.3310
Sherman, D. J., Li, B., Ellis, J. T., & Swann, C. (2017). Intermittent aeolian saltation: A protocol for quantification. *Geographical Review*, 1–19.
Sherman, D. J., Li, B., Farrell, E. J., Ellis, J. T., Cox, W. D., Maia, L. P., & Sousa, P. H. G. O. (2011). Measuring aeolian saltation: A comparison of sensors. *Journal of Coastal Research*, *59*, 280–290. https://doi.org/10.2112/SI59-030.1
Sørensen, M. (2004). On the rate of aeolian sand transport. *Geomorphology*, *59*(1-4), 53–62. https://doi.org/10.1016/j.geomorph.2003.09.005

Sterk, G., Jacobs, A. F. G., & Van Boxel, J. H. (1998). The effect of turbulent flow structures on saltation sand transport in the atmospheric boundary layer. *Earth Surface Processes and Landforms*, *23*(10), 877–887. https://doi.org/10.1002/(SICI)1096-9837(199810)23:10<877::AID-ESP905>3.0.CO;2-R

Stout, J. E. (1998). Effect of averaging time on the apparent threshold for aeolian transport. *Journal of Arid Environments*, *39*(3), 395–401. https://doi.org/10.1006/jare.1997.0370

Stout, J. E. (2004). A method for establishing the critical threshold for aeolian transport in the field. *Earth Surface Processes and Landforms*, *29*(10), 1195–1207. https://doi.org/10.1002/esp.1079

Stout, J. E. (2007). Simultaneous observations of the critical aeolian threshold of two surfaces. Geomorphology, drylands: Linking landscape processes to sedimentary. *Environments*, *85*, 3–16. https://doi.org/10.1016/j.geomorph.2006.03.034

Stout, J. E., & Zobeck, T. M. (1997). Intermittent saltation. *Sedimentology*, *44*(5), 959–970. https://doi.org/10.1046/j.1365-3091.1997.d01-55.x

Stull, R. B. (1988). *An introduction to boundary layer meteorology*. Netherlands: Kluwer.

Ungar, J. E., & Haff, P. K. (1987). Steady state saltation in air. *Sedimentology*, *34*(2), 289–299. https://doi.org/10.1111/j.1365-3091.1987.tb00778.x

van Boxel, J. H., Sterk, G., & Arens, S. M. (2004). Sonic anemometers in aeolian sediment transport research. *Geomorphology*, *59*(1-4), 131–147. https://doi.org/10.1016/j.geomorph.2003.09.011

Walter, B., Horender, S., Voegeli, C., & Lehning, M. (2014). Experimental assessment of Owen's second hypothesis on surface shear stress induced by a fluid during sediment saltation. *Geophysical Research Letters*, *41*, 6298–6305. https://doi.org/10.1002/2014GL061069

Webb, N. P., Galloza, M. S., Zobeck, T. M., & Herrick, J. E. (2016). Threshold wind velocity dynamics as a driver of aeolian sediment mass flux. *Aeolian Research*, *20*, 45–58. https://doi.org/10.1016/j.aeolia.2015.11.006

Wiggs, G. F. S., Atherton, R. J., & Baird, A. J. (2004). Thresholds of aeolian sand transport: Establishing suitable values. *Sedimentology*, *51*(1), 95–108. https://doi.org/10.1046/j.1365-3091.2003.00613.x

Wiggs, G. F. S., Baird, A. J., & Atherton, R. J. (2004). The dynamic effects of moisture on the entrainment and transport of sand by wind. *Geomorphology*, *59*(1-4), 13–30. https://doi.org/10.1016/j.geomorph.2003.09.002

Zingg, A. W. (1953). Wind-tunnel studies of the movement of sedimentary material. *Proceedings of the 5th Hydraulics Conference Bulletin*, *34*, 111–135.